

MSc Physics and Astronomy
Master's Thesis

**Building Position Sensing System for the
Reference Mass of OmniSens**

- a Potential Technology for Einstein Telescope at Low Frequency Science

by
Zhao-Qing Lin
13678671

Supervisor: Dr. C. Mow-Lowry
Second Examiner: Dr. ing. M.G. van Beuzekom
Daily Supervisor: Dr. M. Valentini
Date: February 11, 2024
Credits & Period: 60 ECTS, September 2024 –August 2025

Abstract

Gravitational waves reveal hidden aspects of the universe beyond the reach of other cosmic messengers, yet their detection demands extreme sensitivity. Following the success of LIGO and Virgo, a next generation gravitational wave detector, the Einstein Telescope, aims to achieve greater sensitivity and longer observation time, particularly at low frequencies. This will enable the detection of more massive and earlier cosmic events, leading to breakthroughs in astrophysics and fundamental physics.

To meet these challenges, the OmniSens project introduces a fundamentally new concept: a six-degree-of-freedom inertial isolation system inspired by a drag-free control scheme, that simultaneously achieves high sensitivity at low measurement frequencies, with the benefit of tilt-to-translation decoupling, low force noise, and small dynamic range. Its sensitivity improvement of OmniSens beyond the-state-of-art is guaranteed by a precise position sensing scheme, led by Homodyne Quadrature Interferometers (HoQIs) with other sensors for broadband sensing of the reference mass.

This work focuses on the combination use of two sensors surrounding the reference mass: HoQIs for inertial readout and a capacitive position sensor (CPS) for locating the centre position of the end mass of the reference mass within the sensing frame. The CPS was developed from scratch, and a static performance test was performed in air for one horizontal degree of freedom. It achieves absolute position sensing with an optimized noise floor below $7 \times 10^{-8} \text{ m}/\sqrt{\text{Hz}}$ at 0.1 Hz, and its voltage-to-position transfer function is independent of the output cabling. The result validates the success of the CPS-HoQIs sensing approach in meeting OmniSens' operation goals. Working conditions, potential malfunction mechanisms, and directions for future investigation are also discussed.

Contents

1	Introduction	2
1.1	Gravitational Waves Physics	2
1.2	Ground Based Gravitational Waves Detection	3
1.3	Low Frequency Science and the Einstein Telescope	6
2	The OmniSens Project	8
2.1	Design of the OmniSens	8
2.2	Control and Sensing	10
3	Displacement Sensors for the End Mass	11
3.1	Experimental Setup	12
3.2	Data Acquisition	13
3.3	The Capacity Position Sensor (CPS)	17
3.3.1	Analytical Model and Simulation	18
3.3.2	Upgrades of the Setup	24
3.3.3	Performance Test of the CPS	27
3.4	The Homodyne Quadrature Interferometer (HoQI)	30
4	Results	33
4.1	Calibrating the CPS with HoQI	33
4.2	Offset Analysis	34
5	Conclusion	39
Acknowledgements		40
A		45

1 Introduction

The first direct observation of gravitational waves from a binary black hole system was made by Laser Interferometer Gravitational-Wave Observatory (LIGO) and Virgo collaboration in 14th September 2015 [1]. This discovery not only confirmed general relativity's prediction of the existence of gravitational waves, but also provided a new approach of probing the properties of non-linear strong gravitational field dynamics [2].

This chapter first introduces the gravitational waves physics, followed by an overview of ground-based interferometric detectors. The benefits and challenges of low-frequency gravitational wave detection are discussed. Finally, the scientific goals and technical challenges of the Einstein Telescope (ET) are briefly outlined,

1.1 Gravitational Waves Physics

Einstein's theory of general relativity [2] relates the gravity to the curvature of spacetime. In theory, asymmetric variations in the distribution of mass–energy produce distortions in spacetime that propagate through the universe as ripples, known as gravitational waves. The strain of a gravitational wave is defined as the magnitude of the distortion relative to the original spacetime:

$$h(t) = \frac{\Delta L}{L} \quad (1.1)$$

However, gravitational waves from ordinary astrophysical objects are far too weak to be detected by current instruments. One way to overcome this limitation is to search for exceptionally energetic cosmological events. Figure 1.a) shows the frequency spectrum of gravitational waves generated by different cosmological events, together with the planned sensitivity curves of various gravitational wave detectors, illustrating the range of accessible cosmological information. Figure 1.b) presents four types of gravitational waves sources and their characteristics [3]:

- **Compact binary inspiral gravitational waves** are produced by orbiting pairs of massive and dense objects such as binary neutron star (BNS); binary black hole (BBH), and neutron star-black hole binary (NSBH). The signal begins at low frequency during the inspiral phase, with frequency and amplitude increases as the orbit decays, peaks at the merger, and is followed by a ringdown behaviour.
- **Continuous gravitational waves** are expected from a single spinning object such as a neutron star, producing a long-lasting signal with stable frequency and amplitude.
- **Burst gravitational waves** originate from transient event with extreme energy release. Supernova burst is one of the candidates of such gravitational waves sources.

- **Stochastic gravitational waves** are predicted to arise from the superposition of numerous weak gravitational waves signals coming from across the universe, forming a persistent, irregular gravitational waves background.

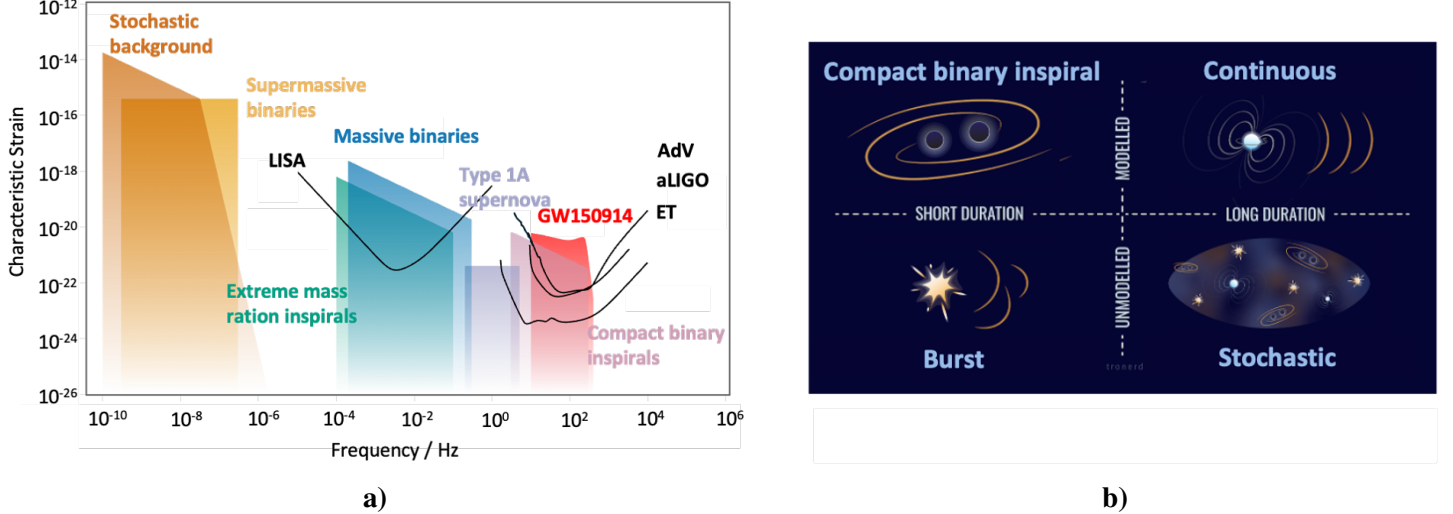


Figure 1: **a)** The frequency spectrum of the gravitational waves generated by different sources, along with their characteristic strain. The planned sensitivity curve of several gravitational waves detectors are plotted. Figure reproduced from [4]. **b)** Four typical types of the gravitational waves sources. Figure adapted from [5].

Among these, compact binary star systems are the primary sources for current detections. As a unique messenger, gravitational waves possess several remarkable properties distinguishing them from other messengers. They convey information with minimal loss and grant access to regions of the universe that are inaccessible to light, including the very early universe. Observing these ripples enables us to identify and study their sources and related astrophysical topics, such as the formation and population of astrophysical objects, the search for dark matter, and the properties of the early universe. For typical gravitational waves sources such as binary star mergers, the waves are emitted before the merger happens. Detecting these signals in advance creates a time window to alert observatories using other messengers to follow up, starting a new era of multi-messenger observations.

1.2 Ground Based Gravitational Waves Detection

Detectable gravitational waves can be modelled by wave-like solutions to the linearized weak-field equations [6]. They behave as transverse waves with two polarization states, exerting stretching and squeezing of spacetime in perpendicular directions, as illustrated in Figure 2.

These spacetime distortions induced by gravitational waves can be detected by precise measurements of the distance between free-floating reference masses [8]. Ground-based detectors use enhanced Michelson interferometry with suspended mirrors to

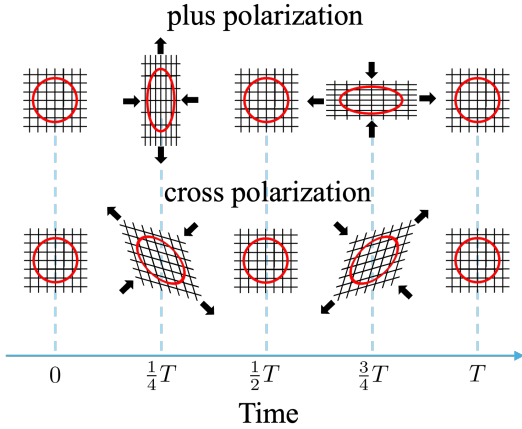


Figure 2: Two polarizations of gravitational waves distorting the spacetime. Figure reproduced from [7].

directly measure these relative changes with high precision. A simple Michelson interferometer, shown in Figure 3, conceptually demonstrated how a gravitational wave signal is converted into a measurable quantity.

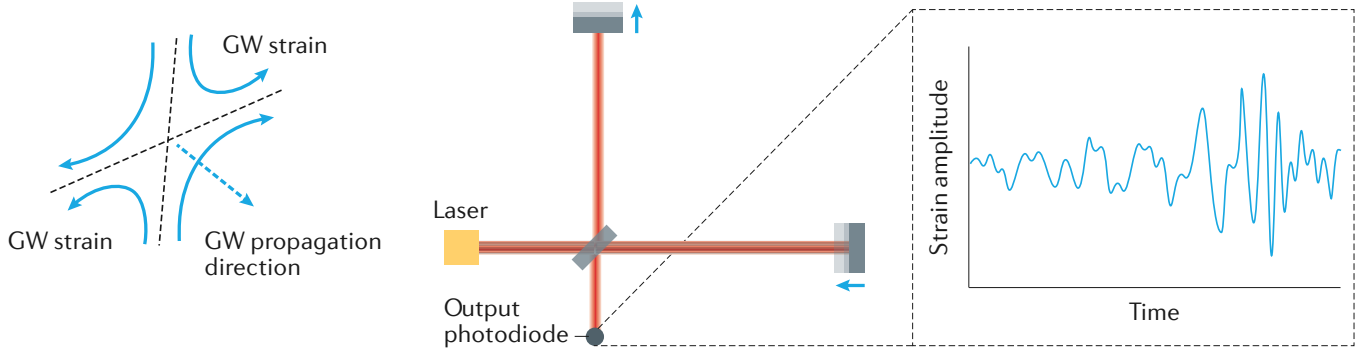


Figure 3: Concept of a simple Michelson interferometer with end mirrors serving as reference masses. When a gravitational wave propagates perpendicular to the plane of the interferometer, one arm shortens while the other lengthens, resulting in a difference in the round-trip travel time of the laser light beams. This time difference produces a phase shift, which is translated into a change in power at the output photodiode after the interference. From this change, the length distortions introduced by the gravitational wave can be reconstructed. Figure reproduced from [9].

In the first direct observation of the gravitational wave, named GW150914, the signal matched the model of the spiral and merger of two black holes ($36 M_{\odot}$ and $29 M_{\odot}$), followed by the ringdown of a single $62 M_{\odot}$ black hole as the result of the merger. The gravitational wave from this colossal astrophysical event induced a length change of approximately 10^{-18} m with respect to the 4 km arms of the two

1 Introduction

ground based interferometer, LIGO Livingston and LIGO Hanford. As shown in Figure 1.a), the strain of gravitational wave signals is incredibly small. Detecting such a subtle change in length requires instruments of extreme precision, making gravitational wave detectors the most sensitive length-measuring instruments ever built.

Constructing and maintaining detectors with this level of sensitivity presents significant technical challenges, particularly the suppression of noise over a wide frequency range. Characterizing noise in gravitational-wave detectors is essential for validating results obtained from passing gravitational waves [10]. The noise budget for the LIGO Hanford Observatory, shown in Figure 4, illustrates the contributions of various noise sources across the frequency spectrum. These include fundamental noises, such as laser shot noise and thermal noise, as well as technical noise arising from detector control systems and environmental disturbances. Suppressing these noise sources improves the signal-to-noise ratio (SNR) of gravitational wave signals, thereby enabling the detection of more and weaker events. The work presented in this thesis specifically focuses on seismic noise at low frequencies.

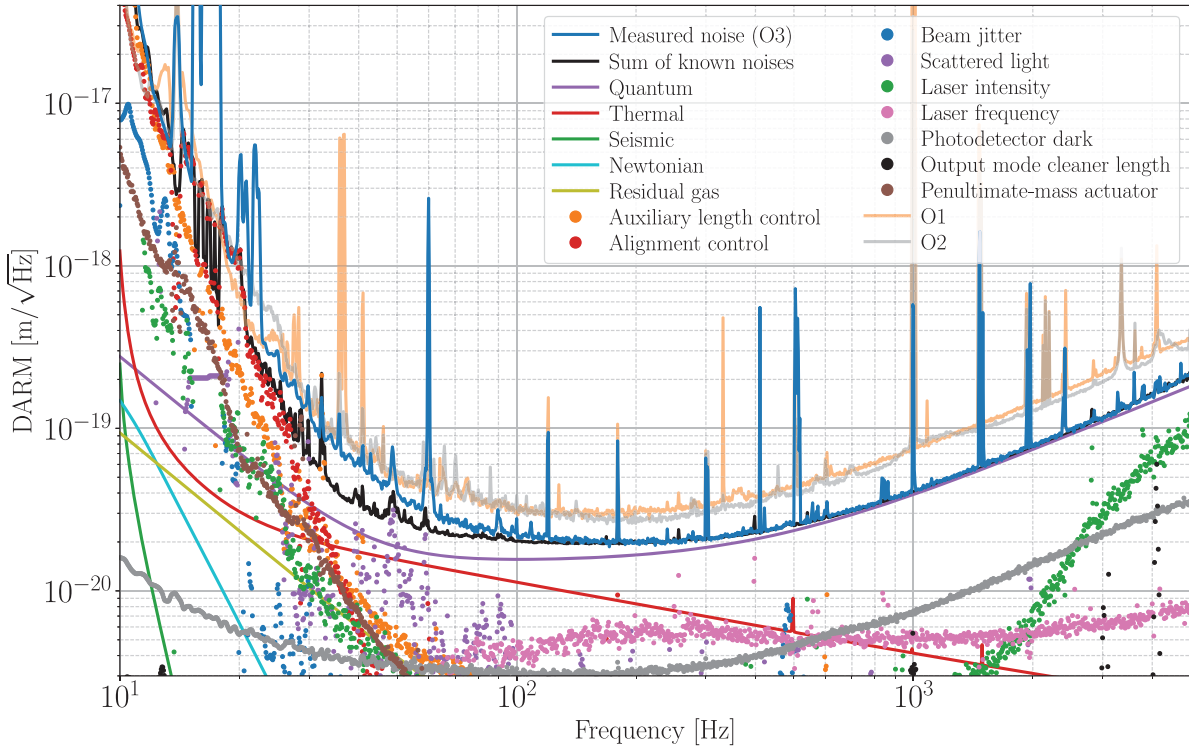
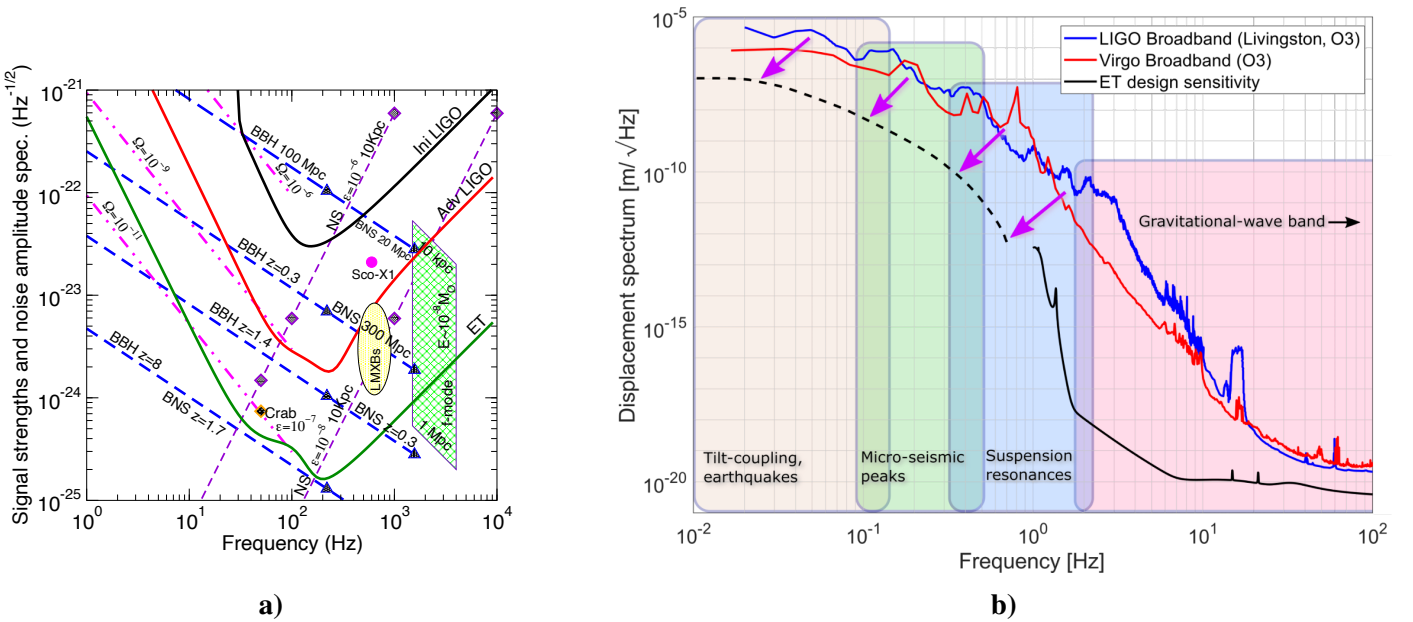


Figure 4: Full noise budget of LIGO Hanford Observatory (LHO), with solid lines representing the calculated noises and dot lines representing the measured contributions. The instrument noise floors for previous observing runs are also plotted. Figure reproduced from [11].

1.3 Low Frequency Science and the Einstein Telescope

Low-frequency gravitational-wave detection is of great scientific importance. Such waves carry information from the early universe at higher redshift, and binary systems with more massive objects [12]. The signal strengths from various gravitational waves sources, compared with the noise amplitude spectrum of three gravitational detectors, as shown in Figure 5.a), illustrating which sources are detectable above noise. Early detection at low frequencies also extends the observation time within the detector’s sensitivity band of binary mergers.



a)

b)

Figure 5: **a)** Noise amplitude spectrum of three generations of ground-based interferometers, along with the expected amplitude spectrum of various narrow and broad-band astrophysical sources. Figure reproduced from [13]. **b)** Comparison of LIGO and Virgo performance during the O3 observing run with ET design sensitivity, including a breakdown of the dominant seismic noise sources across different frequency bands highlighted in coloured boxes. An improvement of approximately 10^6 is expected at 3 Hz. The dash line and arrows indicate the level of improvement required for ET to achieve its sensitivity goal using new technologies. Figure reproduced from [14].

However, current terrestrial detectors are heavily limited below 10 Hz by an effect referred to as the “seismic wall”, where seismic noise and Newtonian noise, the seismic-wave-induced gravitational disturbances, set the sensitivity limit in low frequency range [15]. As a result, the observation rate and SNR for many highly interesting sources in low frequency range remain too low within the current detection range [16].

The Einstein Telescope (ET), a next generation gravitational wave detector, aims

1 Introduction

to push the “seismic wall” towards lower frequency and reduce the noise floor to achieve order-of-magnitude improvement in sensitivity relative to the design sensitivity of Advanced Virgo and Advanced LIGO, as compared in Figure 5.b), and extend the detection band down to 3 Hz. New technologies are required to suppress low-frequency noise, including constructing the ET underground and employing cryogenic systems to reduce the impact of thermal noise.

The research group in which I conducted my master’s project is developing a new technology to mitigate seismic noise, with a particular focus on reducing tilt-to-horizontal coupling.

2 The OmniSens Project

To achieve the ambitious goals of ET, particularly in the low-frequency range, cutting-edge seismic isolation techniques are needed to push the “seismic wall” to lower amplitudes and frequencies.

OmniSens [17] is such a project providing a first-stage seismic isolation for the gravitational waves detector, enabling ET to detect and distinguish astrophysical signals of interest down to 3 Hz. It is a novel six-degree-of-freedom interferometric inertial isolation system that utilizes a drag-free control scheme, making it among the world’s most sensitive inertial sensors.

2.1 Design of the OmniSens

OmniSens is an inertial isolation that is conceptually simple but fundamentally new in ground-based gravitational wave detectors. It employs a softly suspended reference mass, and transfers its inertial stability to the six-axis active platform through a robust control and sensing system. The active platform can be served as an quiet environment that enables the reference mass to approximate free-floating on top of it.

OmniSens incorporates two stages of passive filtering and a drag-free control scheme with their location labelled in Figure 8. A CAD rendering of the OmniSens is shown in Figure 6, with inner layer structures on the right. Stage 0 is the base that is attached to the ground. Three supports fixed on Stage 0 are equipped with titanium blades and flexures, and the active components enabling Stage 1 to move freely in six degree-of-freedom. Stage 1 is suspended from Stage 0 using the blade-springs and is actively controlled to follow the reference mass. On the top of Stage 1 is a breadboard that serves as an “optical bench”. Mounted on the breadboard are the tripod suspending the reference mass, the sensor and actuator frames surrounding the ends of reference mass (end mass), and mass blocks used to balance the active platform.

Lowering the resonance frequency helps to mitigate vibrations in the same degrees of freedom, but vibrations can leak to other degree of freedom through coupling. When suppressing the ground motion, the most challenging issue is the frequency-dependent coupling of vertical rotation to horizontal translation induced by gravity, naming tilt-horizontal coupling. This effect introduces noise that dominates at frequency goes below 0.1 Hz [18]. OmniSens provides an effective solution to this problem and addresses other critical challenges in terrestrial low-frequency inertial isolation, including large forces acting on the reference mass, sensing and control noise, and the large dynamic range.

The reference mass is geometrically large and radially symmetric, with most of its mass concentrated at the ends of its three arms. The properties of the reference and fibre are shown in Figure 7. This configuration results in a moment of inertia sufficient to achieve a tilt resonant frequency of approximately 5 mHz, well below the frequency of the horizontal pendulum modes, enabling the inertial sensors to

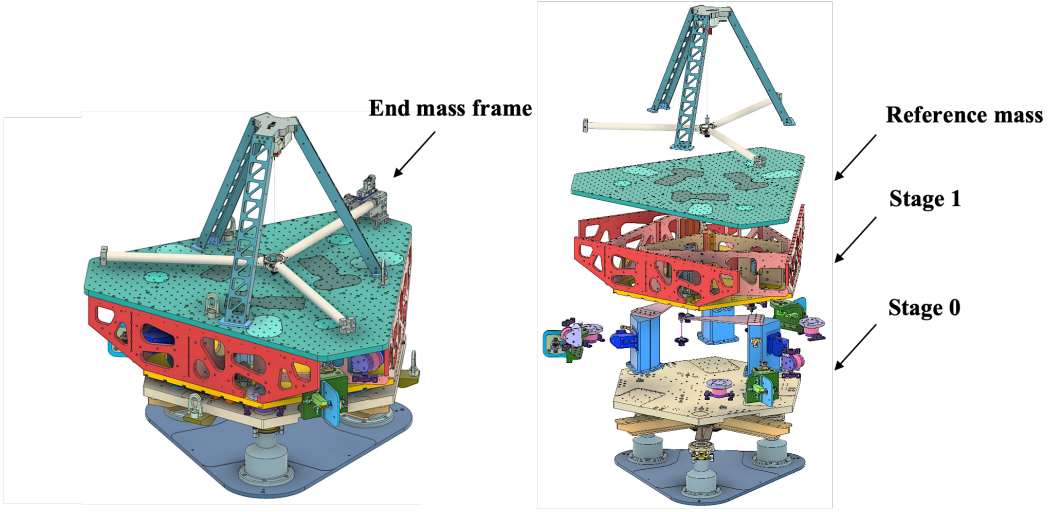


Figure 6: A CAD rendering of OmniSens, with its layered structure shown on the right. From top to bottom, the components are: a three-arm reference mass suspended by a silica fibre; the active platform (Stage 1); and the base (Stage 0), which is attached to the ground.

distinguish and suppress the tilting respect to the $x - y$ plane. By suspending the reference mass near its centre of mass from a fused silica fibre with low thermal noise and low stiffness in horizontal rotation, all degrees of freedom are nearly equally well isolated. This design intrinsically reduces cross-coupling, and minimizes the force noise and dynamic range of sensors for the control and sensing systems.

Design parameter	Value
Reference mass radius	0.815 m
Reference mass	5.1 kg
Rotational inertial (R_x, R_y)	1.0 kg m^2
Rotational inertial (R_z)	1.862 kg^2
Length target for pulled fibre	0.675 m
Diameter target for pulled fibre	0.2 mm
Bulk silica loss angle	$1.0 \times 10^{-9} \text{ rad}$
Height of the tripod	0.70 m

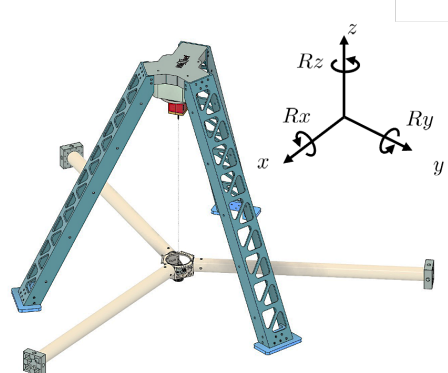


Figure 7: A CAD rendering of OmniSens reference mass and its suspension, with their properties listed in the table on the left.

OmniSens will be installed in a clean vacuum chamber to mitigate the effects of thermal fluctuations and air disturbances affecting the optical sensors and the reference mass. In the future, a thermal shield will be housed around the reference mass, providing further isolation from temperature-induced imbalance.

2.2 Control and Sensing

The control scheme in OmniSens is inspired by drag-free satellites, such as the Laser Interferometer Space Antenna (LISA) [19]. The principle is to maintain a cage at a fixed position relative to a free floating reference mass inside the cage. In a noisy environment, the inertial stability of the reference mass propagates to the cage, and by placing the reference mass inside such a stable cage, the transmission of some external accelerations gets further suppressed to the reference mass.

To adapt this control strategy onto OmniSens, there are three sets of sensors and two sets of actuators on top of the passive suspensions. The active platform serves as the cage, and the relative position of the reference mass is omni-directionally sensed by high resolution sensors located on the active platform. A high-gain closed-loop holds the active platform still to a working position that minimizes the non-linearity of the mechanical response.

See Figure 8 for the positions and 3D rendering of the control and sensing structures. Two sets of conventional displacement sensors are combined to position the reference mass. The Birmingham Optical Sensors and Electromagnet Motors (BOSEM) in Figure 8.B) sense the distance between the ground and the active platform, and Capacitive Position Sensors (CPS) in Figure 8.A) sense the absolute distance between the reference mass and the active platform. A set of interferometers, Homodyne Quadrature Interferometer sensors (HoQIs) in Figure 8.A) sense the inertial motion of the reference mass. Large electromagnetic coils in Figure 8.B) drive the active platform to follow the reference mass, while electrostatic drivers (ESD) in Figure 8.A) provide a low noise fine control to compensate for drift of the reference mass caused by possible noise mechanisms such as thermal gradients, in six-degree-of-freedom at lower frequencies. Together, these two actuators establish a quiet operational cycle for seismic noise isolation, requiring only a small dynamic range.

In the end-mass sensing system, each of the three end masses must be equipped with well-aligned CPS–HoQI sensor pairs in both the horizontal and vertical directions to locate the end mass within the sensing frame and preserve its inertial stability. Whenever a new equilibrium of the reference mass is established, the CPS is used to identify its new null point by driving the active platform to position the end mass at the CPS sensing centre. The HoQIs then measure the inertial motion of the active platform relative to the reference mass with high sensitivity.

HoQI is the key to the OmniSens’ performance, since it preserves the lowest noise across the entire frequency range of interest as demonstrated in Figure 9. At 0.1 Hz, below which the tilt-to-horizontal coupling becomes dominate, the displacement noise of the optimized CPS in Section 3.3.2 is $8 \times 10^{-8} \text{ m}/\sqrt{\text{Hz}}$, and HoQI’ noise is $1 \times 10^{-12} \text{ m}/\sqrt{\text{Hz}}$, yielding a 10^5 improvement on the sensitivity. When used to measure the inertial movement of the reference mass, the noise from HoQIs becomes the final local sensor noise injected into the active control loop, ultimately setting the constraints for OmniSens’ sensitivity.

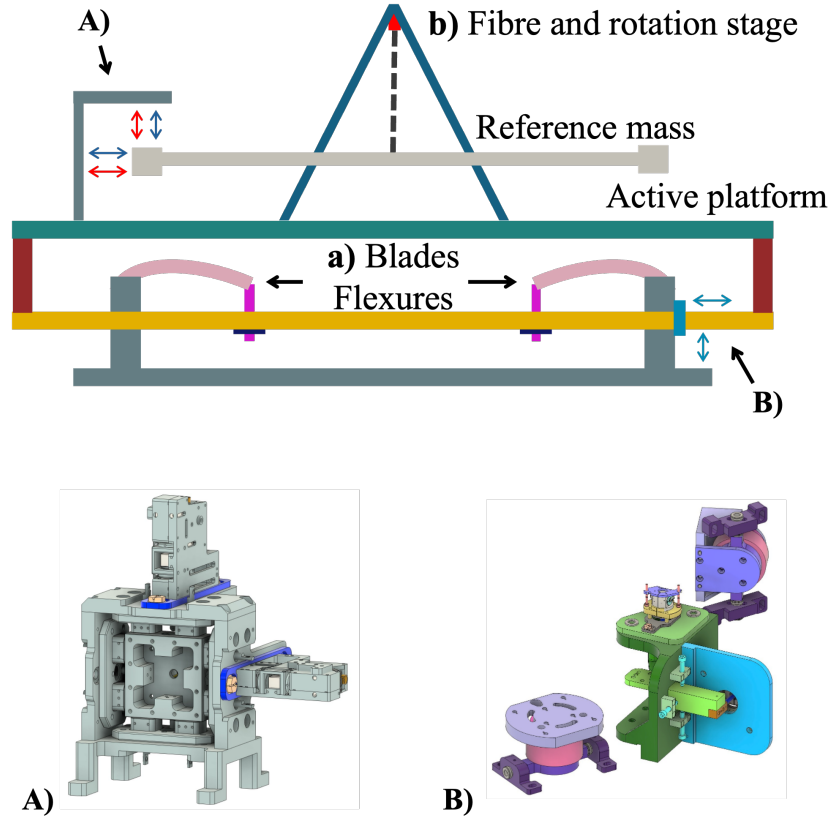


Figure 8: Simplified, not-to-scale 2D schematic of the OmniSens design, with passive isolation labelled as **a**) and **b**), sensors and actuators labelled as **A**) and **B**).

a) Three blades-springs system consisting of Titanium blades and flexures suspends the active platform from the ground.

b) The reference mass is suspended from a rotation stage, which is mounted on the top of the tripod, by a low thermal noise silica fibre. The rotation stage is a stepper motor used to correct the torsional drift of the reference mass.

A) One of the three end masses, with its frame fixed to Stage 1. Two HoQIs and eight CPS electrodes are mounted on the same frame to measure the absolute position of the end mass relative to the frame. The electrostatic drive (ESD) uses the same electrodes to actuate the reference mass suspension.

B) BOSEM and coils, attached to Stage 0, measure the relative position between the platform and the ground, and drive the platform to follow the reference mass.

3 Displacement Sensors for the End Mass

Section 2.2 introduced the overall working principle of the active isolation in OmniSens. A sensing system capable of measuring the relative motion between the

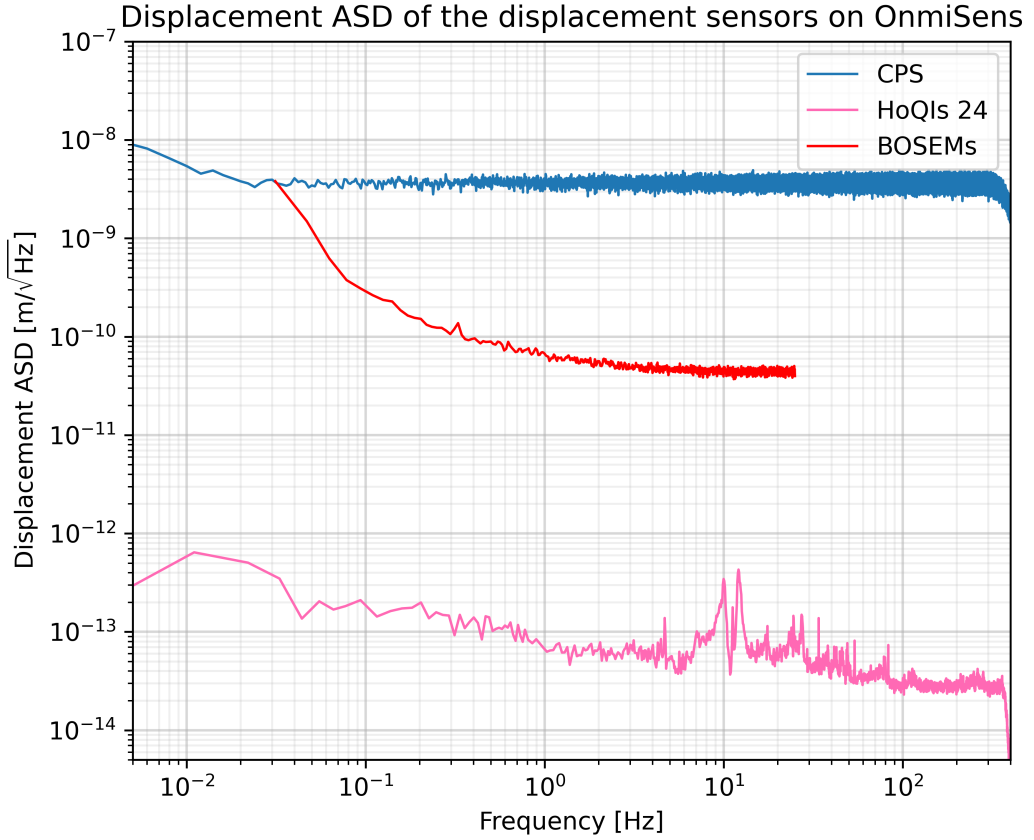


Figure 9: Displacement noise spectrum of three displacement sensors on OmniSens. The CPS data was obtained using 5 m cables with the updated board. The HoQIs 24 data is provided by [10], and BOSEM data is from LIGO A+ upgrade [20].

reference mass and the active platform in all six degrees of freedom is the start for implementing the drag-free control strategy. This is performed by the CPS and HoQIs shown at the each end mass Figure 8.A). In this chapter, I will present the design of two displacement sensors. Since the CPS for OmniSens was developed from scratch, this chapter investigates its analytical transfer function, simulations, upgrades, and preliminary calibration in one translational degree of freedom. The experimental setup and data acquisition (DAQ) system are also described.

3.1 Experimental Setup

Since three end masses and their surrounding sensor frames are identical and located at the ends of arms with 120° rotational symmetry, we can simplify the OmniSens' reference mass position sensing by focusing on one end mass system. In the OmniSens' design, the six-degree-of-freedom are well decoupled, thus one-dimensional displacement sensing provides significant insights to the working scenario. Figure 10.a) shows the experimental setup of the end mass system. A connection struc-

ture, shown in the green frame in Figure 10.a), attaches a protophyte of end mass cube made from aluminium, which will be replaced with bronze in the operational OmniSens, to the cart on the micrometric screw. The micrometric screw allows preliminary calibration of the CPS before switching to HoQI and also provides a one-dimensional translation to simulate operational scenario.

From the CAD design, Figure 10.b), two HoQIs are mounted on the outer side of the frame, one in the horizontal direction and the other one in the vertical direction. Eight CPS electrodes are fixed to the inner side of the frame, with two parallel electrodes attached to each of its four sides. Two pairs of electrodes on opposite sides form one CPS sensor.

On each side of the frame, as shown in the layered structure in Figure 11 (right), a metal stop is positioned between the two electrodes. This metal stop set the maximum moving range x_{move} of the end mass, preventing it from hitting the electrodes. The electrodes are mounted to the frame from a plate using insulating spacers, and each electrode is connected to the output cables through a connection spigot, which leads to the CPS electronic board in Figure 15.a). If the end mass touches the stops, it will be shorted, causing the output signal to drop suddenly to zero, which indicates that the end mass has reached its mechanical limits.

The two HoQIs in the end mass system have identical setups. A layered setup of horizontal HoQI is shown in Figure 11 (left). Two cams on the adjusting plate are used to move the HoQI within the frame plane. By rotating the cams, optimal interference with the retroreflector inside the end mass can be achieved, resulting in the highest fringe visibility.

The geometric parameters of the setup excluding HoQIs and the vertical CPS electrodes are labelled in Figure 12, with their values summarized in Table 1. The gaps between the two planes of the electrode and the end mass are labelled as x_1 on the left and x_2 on the right. When the end mass is sitting on the centre position of the electrodes, $x_1 = x_2 = x_0$, thus $x_0 = 1.15 \text{ mm}$. If the end mass is displaced by x to the right away from the central position, the gaps become $x_1 = x_0 + x$ and $x_2 = x_0 - x$. The maximum moving range of the end mass $x_{\text{move}} = l_{\text{stop}} - l_{\text{EM}} = 1.48 \text{ mm}$. Apart from l_{stop} , which was measured using the micrometric screw, all the other parameters were measured using a caliper with a resolution of 0.01 mm.

The distances between the electrodes and the frame l_L and l_R differ from the designed values, resulting a 15% discrepancy in x_0 between the design and the actual setup. Several factors could contribute to the discrepancy, such as compound machining tolerance of the electrodes, plates and insulating plates, and eventual compression of the insulating plates during the assembly procedure.

3.2 Data Acquisition

The data acquisition system designed for this experiment, along with the OmniSens project, is based on software and hardware architecture used in Virgo. This includes

3 Displacement Sensors for the End Mass

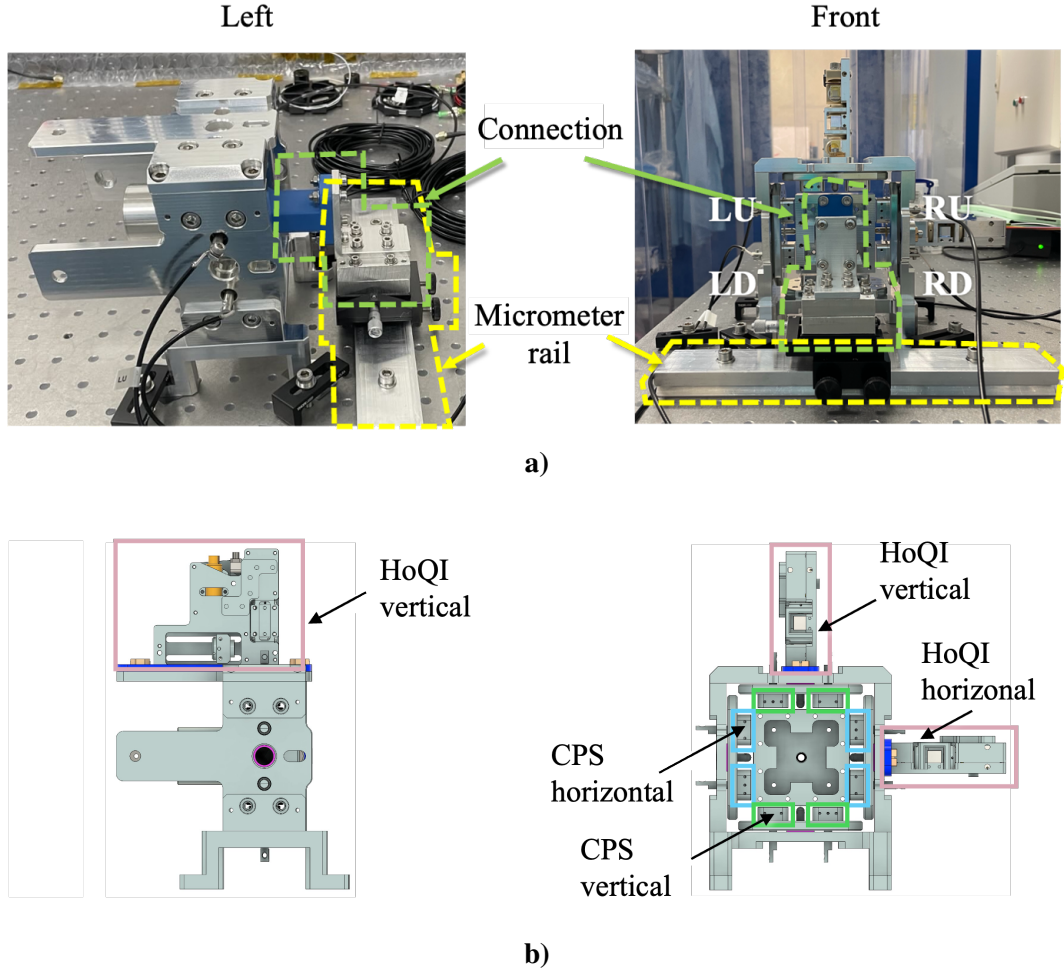


Figure 10: **a)** The end mass and frame setup viewed from the left and front sides. One vertical HoQIs and one horizontal HoQIs are installed. The yellow frame shows the micrometric screw fixed on the rack with a cart on top of it, which has a resolution of 0.01 mm. The green frame shows the connection between the end mass cube and the cart. Four cables connected to the electrodes in the horizontal plane are labelled LU (Left Up), LD (Left Down), RU (Right Up), and RD (Right Down). The signal is injected in the test mass through a capacitor, emulating what will be done in the final setup in order to not have any direct contact between test mass and surrounding environment other than the silica fibre. **b)** A CAD rendering of the end mass and sensing frame from the left and front. The vertical and horizontal CPS and HoQIs are highlighted.

data processing packages such as Virgool [21], GWpy [22], and a real-time digital control system called Algorithms for Control and Locking (ACL) [23].

Part of the DAQ hardware setup of this experiment is shown in Figure 13. The Virgo DAQ box [24] serves as a DAQ interface. It receives commands from a real-

3 Displacement Sensors for the End Mass

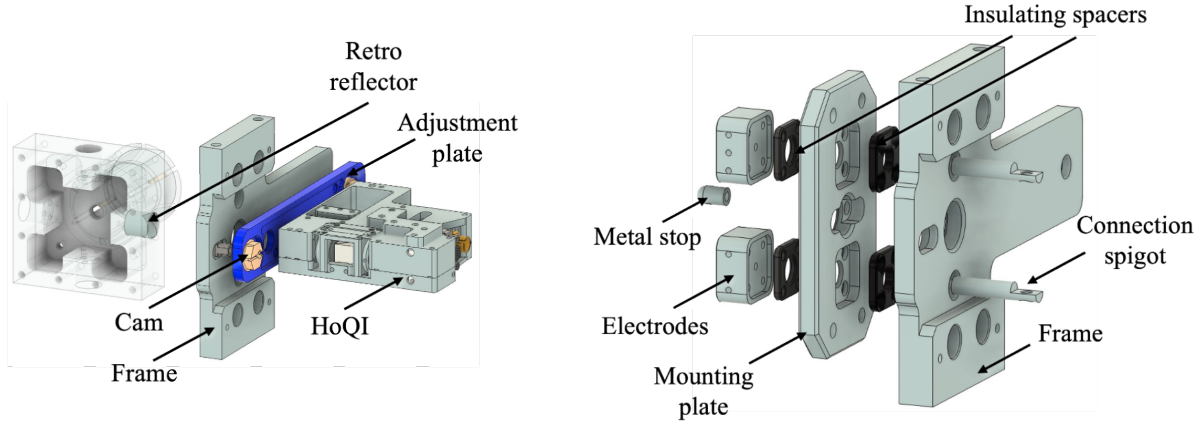


Figure 11: Setup for horizontal HoQI (left) and the horizontal CPS on single side (right).

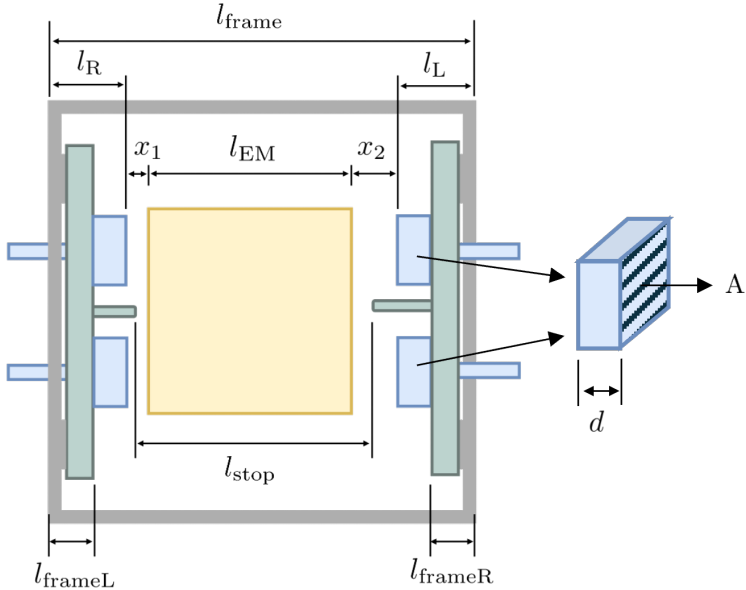


Figure 12: A 2D scheme of the CPS and end mass system. HoQIs and the vertical CPS electrodes are not shown. Geometric parameters are labelled, and their descriptions and values of the parameters are summarized in Table 1.

time computer (RTPC), which is connected to the internet, enabling remote control and data acquisition. The DAQ box hosts the digital-to-analog converter (DAC) and the analog-to-digital converters (ADCs) for the CPS, and the ADC for HoQIs. The HoQIs preamplifiers are transimpedance amplifiers that convert the photodiodes currents into voltages. The SR560 preamplifier amplifies the CPS input signal from the DAC. A Moku:Pro was used for multiple quick checks, including monitoring the fringe visibility of HoQIs during tuning the interference on the frame. The power supply is set to 5V to drive the amplifiers on the electronics board shown in Figure 15.a). The electronics board is the main module to process the output signals

3 Displacement Sensors for the End Mass

Parameter	Description	Value (Measured)	Value (Designed)
l_{frame}	Width of the outer frame	132.00 mm	132.00 mm
l_{frameL}	Thickness from the frame to mounting plate (left)	20.00 mm	20.00 mm
l_{frameR}	Thickness from the frame to mounting plate (right)	19.99 mm	20.00 mm
l_L	Distances between the electrodes and the frame (left)	29.83 mm	30.00 mm
l_R	Distances between the electrodes and the frame (right)	29.87 mm	30.00 mm
l_{EM}	Width of the end mass cube	70.00 mm	70.00 mm
l_{stop}	Distance between two metal stops	71.48 mm	71.50 mm
d	Thickness of one electrode	10.00 mm	10.00 mm
A	Area of one electrode plate	—	4.50 cm ²

Table 1: The geometry parameters and of the end mass system without HoQIs and the vertical CPS. The measured values and designed values are compared in the table.

from the four electrodes and provide a stable gain G from the voltage readout to the displacement x that is independent of the cabling.

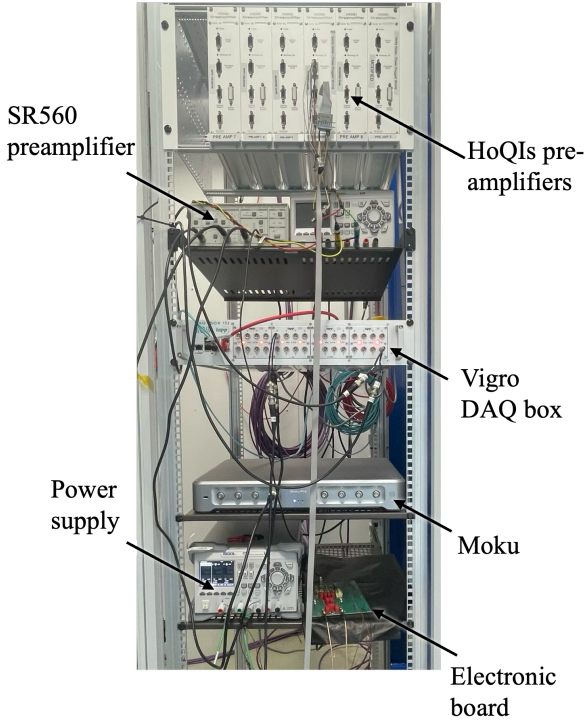


Figure 13: The DAQ setup for the CPS and HoQIs in the lab. The RTPC is connected from outside the lab.

3.3 The Capacity Position Sensor (CPS)

The CPS is a mature technology widely used in position measurement in ground-based [18] and space-based gravitational waves detectors [25]. It employs a straightforward differential sensing method: the electrode plate and the target form a capacitor whose impedance depends on the distance between their surfaces. By placing the target in between a pair of electrodes with a fixed separation, the impedances of two capacitors, as well as their difference, have a one-to-one mapping to the target's position. Here we describe this voltage-to-position relationship as a transfer function from voltage to the position with a gain of G . Thus, when applying a voltage to the end mass, the position of the end mass can be determined using the system's transfer function $x = GV_{\text{CPS}}$. The gain G would only depend on the displacement x , assuming a fixed setup configuration and the input voltage.

In the OmniSens project, if the end mass has a translational displacement x from the sensing centre, the capacities of two capacitors pairs are:

$$C_{LU} = C_{LD} = \frac{\epsilon A}{x_0 + x}, \quad C_{RU} = C_{RD} = \frac{\epsilon A}{x_0 - x} \quad (3.1)$$

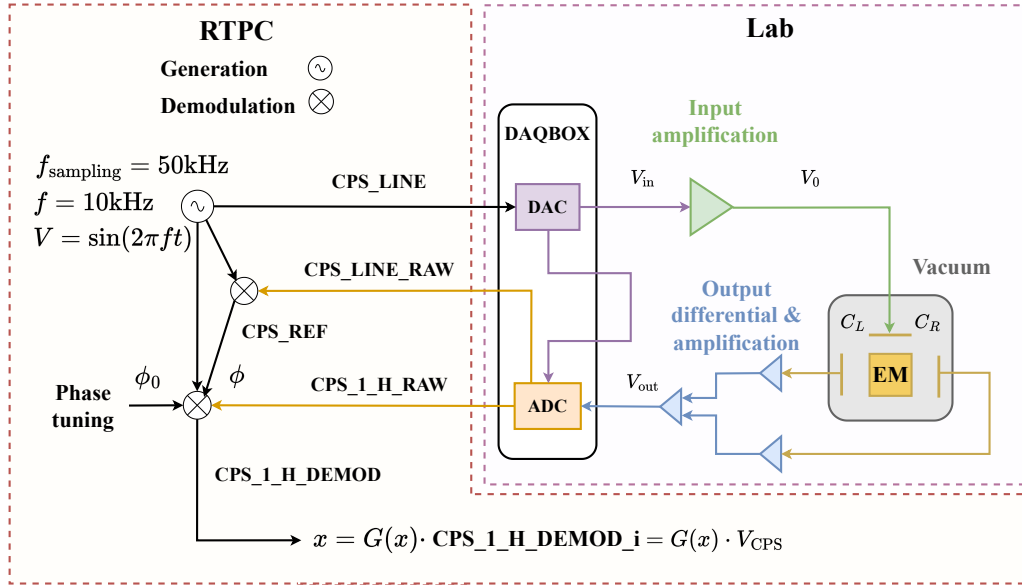


Figure 14: CPS setup and DAQ system.

A simplified schematic of the CPS working flow in the horizontal direction is shown in Figure 14. A digital source signal CPS_LINE is generated from the RTPC as a normalized sinusoid wave $\sin(2\pi ft)$, with frequency $f = 10 \text{ kHz}$ and sampling frequency $f_{\text{sampling}} = 50 \text{ kHz}$. The DAC converts the CPS_LINE into a differential analog signal V_{in} and sends it to the SR560. The SR560 preamplifier amplifies the CPS input signal V_{in} from the DAQ box and converts it into an 8.4V peak-to-peak single-ended signal V_0 . The amplitude of V_0 is confirmed both by measurement with

the Moku and by direct input to the ADC. In parallel, the same signal is routed directly to the ADC in the same DAQ box as CPS_LINE_RAW, and is demodulated with the digital CPS_LINE in the RTPC, to obtain a phase delay ϕ only due to the round-trip path from the RTPC to the DAQ box. The signal V_0 then propagates through the end mass system, with the connections shown in Figure 10.a).

The electronics board that receives the output signals coming from the four electrodes is shown in Figure 15.a), with notations explained in Figure 15.b). The output amplifiers on the board provide a total gain of 50 and take the difference between the voltages after C_7 , C_8 and C_9 , C_{10} , producing a signal V_{out} that is later recorded as CPS_1_H_RAW. Here, “1” refers to one specific end mass systems out of three, and “H” denotes the horizontal direction. In this experiment, the horizontal CPS output signal is labelled as CPS_1_H_RAW.

In the RTPC, CPS_1_H_RAW is demodulated with CPS_LINE, including the additional phase delay ϕ and a phase tuning of ϕ_0 . The phase tuning is adjusted to compensate for the phase delay within the end mass system, until the out-of-phase channel of CPS_1_H_RAW remains close zero during the end mass motion. Thus, the final output CPS_1_H_DEMOD_i represents the in-phase channel after demodulation with CPS_LINE, and is denoted as V_{CPS} throughout this thesis.

In this way, we can calibrate the CPS output voltage V_{CPS} with the displacement x . By inverting this calibration, the voltage-to-displacement transfer function of the end mass is obtained: $x = G(x)V_{\text{CPS}}$, making the CPS an absolute position sensor.

Three methods are used to calibrate V_{CPS} to the position x : analytical calculation, simulation and the measurement. In Section 3.3.1, the analytical transfer function $x = G_{\text{ana}}(x)V_{\text{CPS}}$ is derived, including the analysis of the effects of several components with variable impedance. A simulated transfer function is obtained using *LTspice* and compared with the analytical result, along with a polynomial fit for the calibration. In Section 3.3.2, the CPS was calibrated using the micrometric screw, giving a preliminary transfer function. A more precise calibration was performed using HoQI in Chapter 4. By comparing this with the analytical gain $G_{\text{ana}}(x)$, we troubleshoot and updated the electronics board and the cabling to achieve a stable gain and optimized noise performance.

3.3.1 Analytical Model and Simulation

The circuit schematic of the CPS before the amplifiers is shown in Figure 15.b). The input signal $V_0 = 4.2 \sin(2\pi ft) \text{ V}$ with $f = 10 \text{ kHz}$ is injected to the end mass system through a capacitor C_1 . C_2 represents the stray capacitor between the end mass and its surroundings. The four CPS capacitors are C_{LU} , C_{LD} , C_{RU} , and C_{RD} , where C_{LU} and C_{LD} share the potential $V_1 - V_L$ on the left branch, and C_{RU} and C_{RD} share the potential $V_1 - V_R$ on the right branch.

C_3 , C_4 , C_5 , C_6 accounts for the capacitors between the output coaxial cables and the guard, and the voltage applied on them is $(V_L - V_{LC})$ and $(V_R - V_{RC})$ respectively. The buffers in the blue blocks are the major upgrade to the electronics board. These

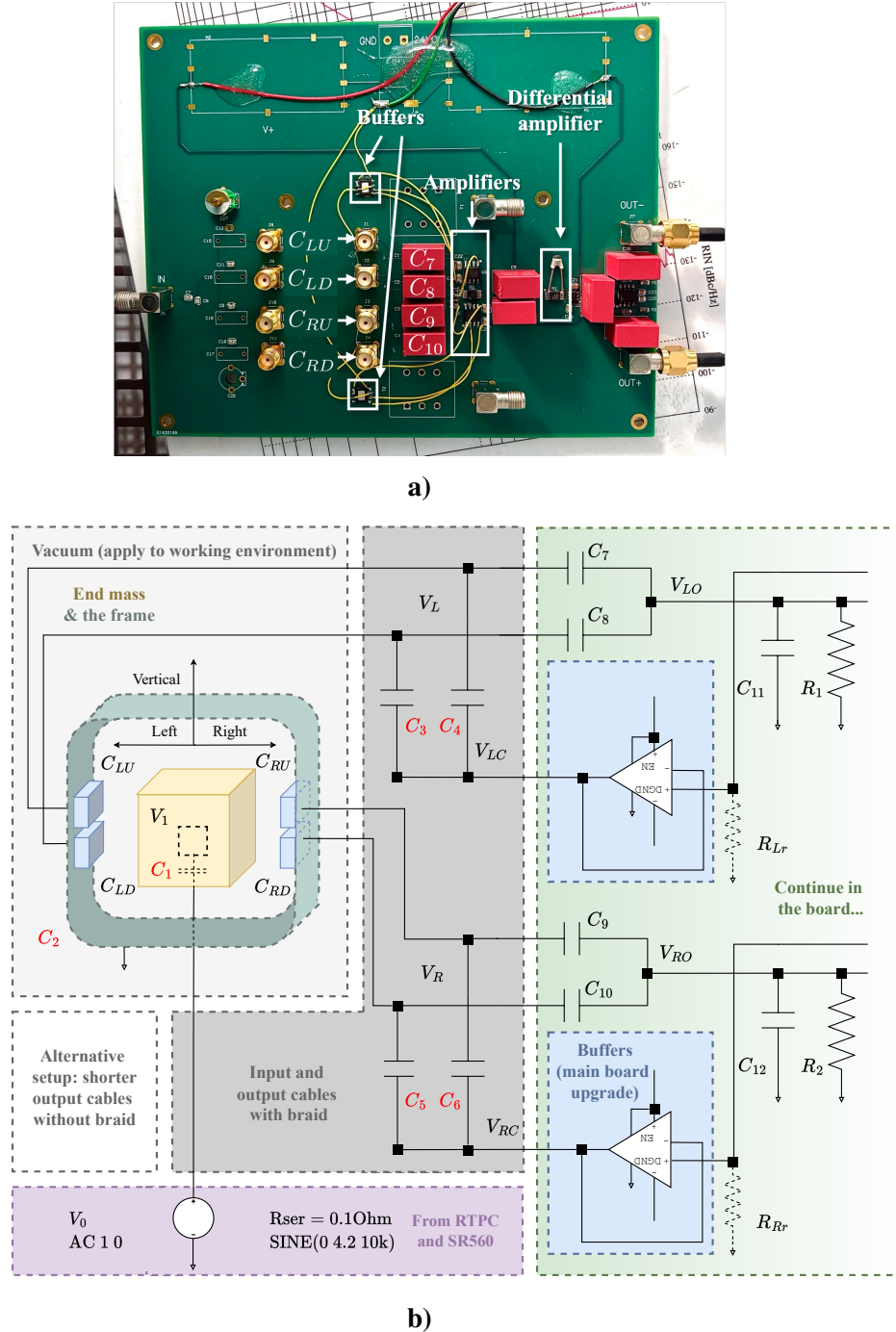


Figure 15: **a)** The electronics board of the CPS. **b)** Schematic of the CPS electronics, excluding the output amplifiers. The main components shown include: the end mass and horizontal CPS, cables with braid, and the electronics board before amplification. Components labelled in red indicate the unknown impedance values, which can only be determined through estimation and curve fitting. A schematic of the full circuit including the amplifiers can be found in Figure 18.a).

buffers eliminate the dependence of gain G on the output cabling, which is verified in both calculation and measurement. Capacitors C_7 , C_8 , C_9 , C_{10} serve as drive biases for the electrostatic actuators that share the same electrodes as the CPS. C_{11} and C_{12} are the capacitors between the board and the ground. R_1 and R_2 are used to divert the DC signal to the ground to prevent amplifier saturation. R_{Lr} and R_{Rr} are reference resistors only used for setting voltage probing points after the buffers for the transfer function calculation, and are assumed to have effectively infinite resistance.

Before proceeding with the calculation, we define several parameters to simplify the derivation. The capacitances of four capacitors for the CPS are:

$$\begin{aligned} C_{LU} &= C_{LD} = C_L = \frac{\epsilon A}{x_0 + x} \\ C_{RU} &= C_{RD} = C_R = \frac{\epsilon A}{x_0 - x} \end{aligned} \quad (3.2)$$

Because of the left branch and the right branch have the same circuit design after the CPS capacitors, defining the following parameters will hugely simplify the calculation:

$$\begin{aligned} C_3 &= C_4 = C_5 = C_6 = C_c \\ C_7 &= C_8 = C_9 = C_{10} = C_s \\ C_{11} &= C_{12} = C_g \\ R_1 &= R_2 = R \\ R_{Lr} &= R_{Rr} = R_\infty = \infty \end{aligned} \quad (3.3)$$

The current flowing through two cables capacitors on the left branch is I_{LC} and through C_7 and C_8 is I_{LO} .

$$\begin{aligned} I_{LC} &= sC_c(V_L - V_{LC}) = \frac{1}{2} \frac{V_{LC}}{R_r} \\ I_{LO} &= sC_s(V_L - V_{LO}) = \frac{1}{2} (sC_g + \frac{1}{R}) V_{LO} \end{aligned} \quad (3.4)$$

On the right branch, I_{RC} flows through C_5 and C_6 , I_{LO} flows through C_7 and C_8 .

$$\begin{aligned} I_{RC} &= sC_c(V_R - V_{RC}) = \frac{1}{2} \frac{V_{RC}}{R_r} \\ I_{RO} &= sC_s(V_R - V_{RO}) = \frac{1}{2} (sC_g + \frac{1}{R}) V_{RO} \end{aligned} \quad (3.5)$$

The relationship of the voltage after cables and the output is:

$$\begin{aligned} V_L &= \frac{1 + 2sR_rC_c}{2sR_rC_c} V_{LC} = \frac{1 + sRC_g + 2sRC_s}{2sRC_s} V_{LO} \\ V_R &= \frac{1 + 2sR_rC_c}{2sR_rC_c} V_{RC} = \frac{1 + sRC_g + 2sRC_s}{2sRC_s} V_{RO} \end{aligned} \quad (3.6)$$

3 Displacement Sensors for the End Mass

Thus we have $V_{LO} = AV_{LC}$ and $V_{RO} = A_{LR}V_{RO}$, in which:

$$\begin{aligned}
 A_{LR} &= \left(\frac{1 + 2sR_rC_c}{2sR_rC_c} \right) \div \left(\frac{1 + sRC_g + 2sRC_s}{2sRC_s} \right) \\
 &= \frac{RC_s + 2sR_rRC_cC_s}{R_rC_c + sRR_rC_gC_c + 2sRR_rC_sC_c} \\
 &\approx \frac{2sRC_cC_s}{C_c + 2sRC_gC_c + 2sRC_sC_c} \\
 &= \frac{2sRC_s}{1 + sRC_g + 2sRC_s}
 \end{aligned} \tag{3.7}$$

The approximation is achieved because of $R_r \rightarrow \infty$, so here we already can see the transfer function is unrelated to the cables C_c . Define the current goes into the left branch and right branch are I_L and I_R respectably:

$$\begin{aligned}
 I_L &= 2sC_L(V_1 - V_L) \\
 &= 2(I_{LC} + I_{LO}) \\
 I_R &= 2sC_R(V_1 - V_R) \\
 &= 2(I_{RC} + I_{RO})
 \end{aligned} \tag{3.8}$$

Find the relationship of V_{LC} to V_1 :

$$\begin{aligned}
 V_1 &= V_L + (I_{LC} + I_{LO})\frac{1}{sC_L} \\
 &= \frac{1 + 2sR_rC_c}{2sR_rC_c}V_{LC} + \frac{1}{2sC_L} \left(\frac{1}{R_r} + \frac{A_{LR}}{R} + sAC_g \right) V_{LC} \\
 &\approx \left[1 + \frac{A_{LR}}{2sC_L} \left(\frac{1}{R} + sC_g \right) \right] V_{LC} \\
 &= \left(1 + \frac{i}{2sC_L} \right) V_{LC} \\
 &= B_L V_{LC}
 \end{aligned} \tag{3.9}$$

in which define $i = A_{LR} \left(\frac{1}{R} + sC_g \right)$ for simplicity. Due to the symmetry:

$$\begin{aligned}
 V_1 &= \left(1 + \frac{i}{2sC_R} \right) V_{RC} \\
 &= B_R V_{RC}
 \end{aligned} \tag{3.10}$$

and $B_L V_{LC} = B_R V_{RC}$. Now find the relationship for V_{LC} and V_{RC} to the source, from the left branch:

$$\begin{aligned}
 V_0 &= V_1 + V_1 \frac{C_2}{C_1} + (I_L + I_R) \frac{1}{sC_1} \\
 &= B_L V_{LC} + \frac{C_2}{C_1} B_L V_{LC} + \frac{i}{sC_1} (V_{LC} + V_{RC}) \\
 &= \left[B_L + \frac{C_2}{C_1} B_L + \frac{i}{sC_1} \left(1 + \frac{B_L}{B_R} \right) \right] V_{LC} \\
 &= D_L V_{LC} \\
 &= D_R V_{RC}
 \end{aligned} \tag{3.11}$$

In summary, the constant parameters A and i are:

$$\begin{aligned}
 A_{LR} &= \frac{2sRC_s}{1 + sRC_g + 2sRC_s} \\
 i &= A_{LR} \left(\frac{1}{R} + sC_g \right)
 \end{aligned} \tag{3.12}$$

and the parameters that are dependent to the displacement x are:

$$\begin{aligned}
 B_L &= \left(1 + \frac{i}{2sC_L} \right) \\
 B_R &= \left(1 + \frac{i}{2sC_R} \right) \\
 D_L &= \left[B_L + \frac{C_2}{C_1} B_L + \frac{i}{sC_1} \left(1 + \frac{B_L}{B_R} \right) \right] \\
 D_R &= \left[B_R + \frac{C_2}{C_1} B_R + \frac{i}{sC_1} \left(1 + \frac{B_R}{B_L} \right) \right]
 \end{aligned} \tag{3.13}$$

Finally, we derive the transfer function from the input signal V_0 to the output signal V_{LO} and V_{RO} for two branches.

$$\begin{aligned}
 \frac{V_{LO}(x)}{V_0} &= A_{LR} D_L(x) \\
 \frac{V_{RO}(x)}{V_0} &= A_{LR} D_R(x)
 \end{aligned} \tag{3.14}$$

Treating the amplifiers and differential amplifiers in the schematic as ideal components, which provide a 50-fold amplification after V_{LO} and V_{RO} , the final output for the CPS system V_{CPS} after demodulation in the RTPC can be expressed as:

$$\begin{aligned}
 V_{CPS} &= 50 \times A |V_0| (D_L(x) - D_R(x)) \\
 &= 50 \times 4.2 \times A (D_L(x) - D_R(x)) [\text{V}]
 \end{aligned} \tag{3.15}$$

In the electronic setup, there are some components that their impedances differ with the surrounding and are unclear, such as C_1, C_2 and cable capacitance C_c :

3 Displacement Sensors for the End Mass

Capacitor	Description
C_1	Capacitance between the input electrode and testmass
C_2	Stray capacitance between the end mass and its surrounding
C_c	Capacitance between the output coaxial cables and the guard

Table 2: The capacitors with non-fixed impedance and their descriptions are listed below. Their influence on the transfer function is discussed in the following sections.

The relationship between the voltage and the displacement, $x = G(x)V_{\text{CPS}}$, is shown in Figure 16, along with the analysis with different values of C_1 , C_2 and C_c . The curve shows a one-to-one map correspondence between the voltage output and the displacement, confirming our CPS design can effectively measure the position of the end mass. The gain $G(x)$ increases when C_1 is smaller or C_2 is larger capacitance, while it remains unaffected by the cable capacitance C_c .

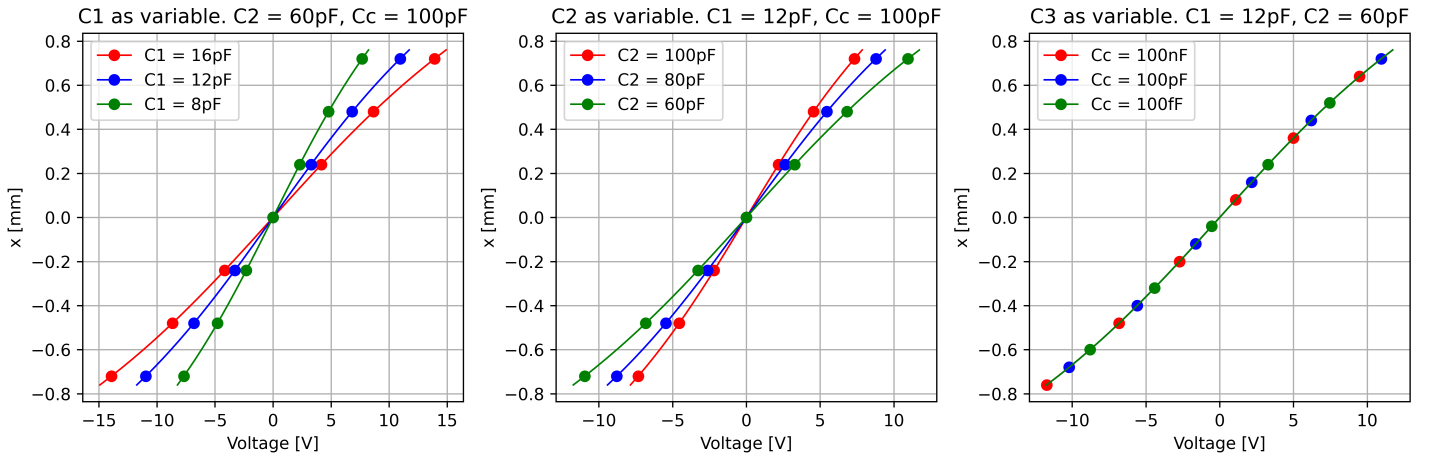


Figure 16: Analysis of the impact of different C_1 , C_2 , and C_c values on the transfer function.

In the experimental setup, C_1 is represented by attaching a 12 pF capacitor to the end mass cube, leaving C_2 as the only variable component influencing the analytical value of gain. For the following simulation and measurement, C_1 is assumed to be fixed at 12 pF. In the OmniSens configuration, C_1 is determined by the injection electrode area and its distance from the reference mass. Due to geometrical reasons and the safety margin in the plate separation, C_1 is unlikely have a capacity larger than 12 pF.

A polynomial cubic fit can provide good approximation for the CPS' behaviour, as shown in Figure 17 of the transfer function. As C_2 increases, the gain gets higher. In the setup of $C_2 = 60$ pF, 80 pF and 100 pF, the corresponding fit for transfer functions are:

$$\begin{aligned}
 C_2 = 100 \text{ pF} : x [\mu\text{m}] &= 110.211 [\mu\text{m}] V_{\text{CPS}} [\text{V}] - 0.224 [\mu\text{m}/\text{V}^3] V_{\text{CPS}}^3 [\text{V}]^3 \\
 C_2 = 80 \text{ pF} : x [\mu\text{m}] &= 91.844 [\mu\text{m}] V_{\text{CPS}} [\text{V}] - 0.128 [\mu\text{m}/\text{V}^3] V_{\text{CPS}}^3 [\text{V}]^3 \\
 C_2 = 60 \text{ pF} : x [\mu\text{m}] &= 73.473 [\mu\text{m}] V_{\text{CPS}} [\text{V}] - 0.065 [\mu\text{m}/\text{V}^3] V_{\text{CPS}}^3 [\text{V}]^3
 \end{aligned} \quad (3.16)$$

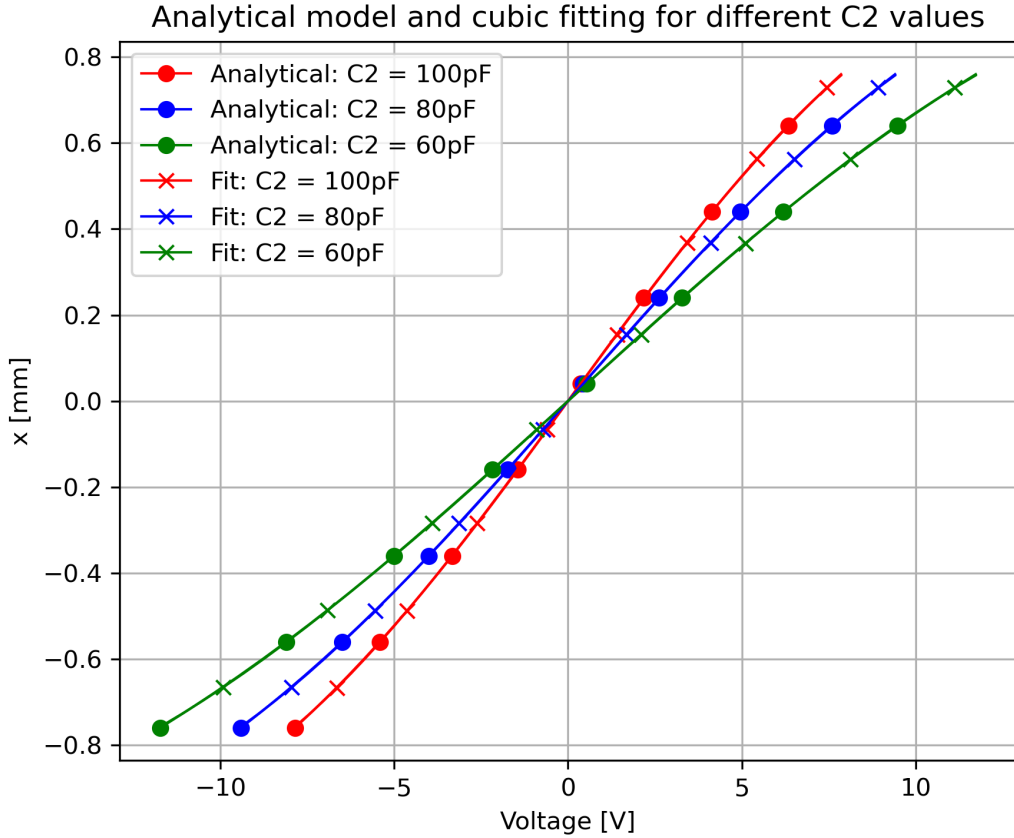


Figure 17: The cubic fits of the transfer function for different C_2 values.

Using the circuit schematic in Figure 18.a), the transfer function was simulated by *LTspice* and compared with the analytical results plotted in Figure 18.b). Considering the electronic components are not ideal in the simulation and will introduce the loss of the signal, the simulation and analytical model highly agree with each other.

For a small displacement of the end mass around the centre, good linearity of the transfer function is preserved. This also benefits the modelling of the electrostatic driver, which shares the CPS electrodes with its control force is non-linearly coupled to the gap between the electrodes plane and the end mass.

3.3.2 Upgrades of the Setup

The gain of the CPS was first roughly estimated by moving the end mass horizontally with the micrometric cart. When a translation displacement δx was measured by the micrometric screw, the output voltage obtained a voltage change δV read from *dataDisplay* [26], which is a data processing and visualizing software developed for

3 Displacement Sensors for the End Mass

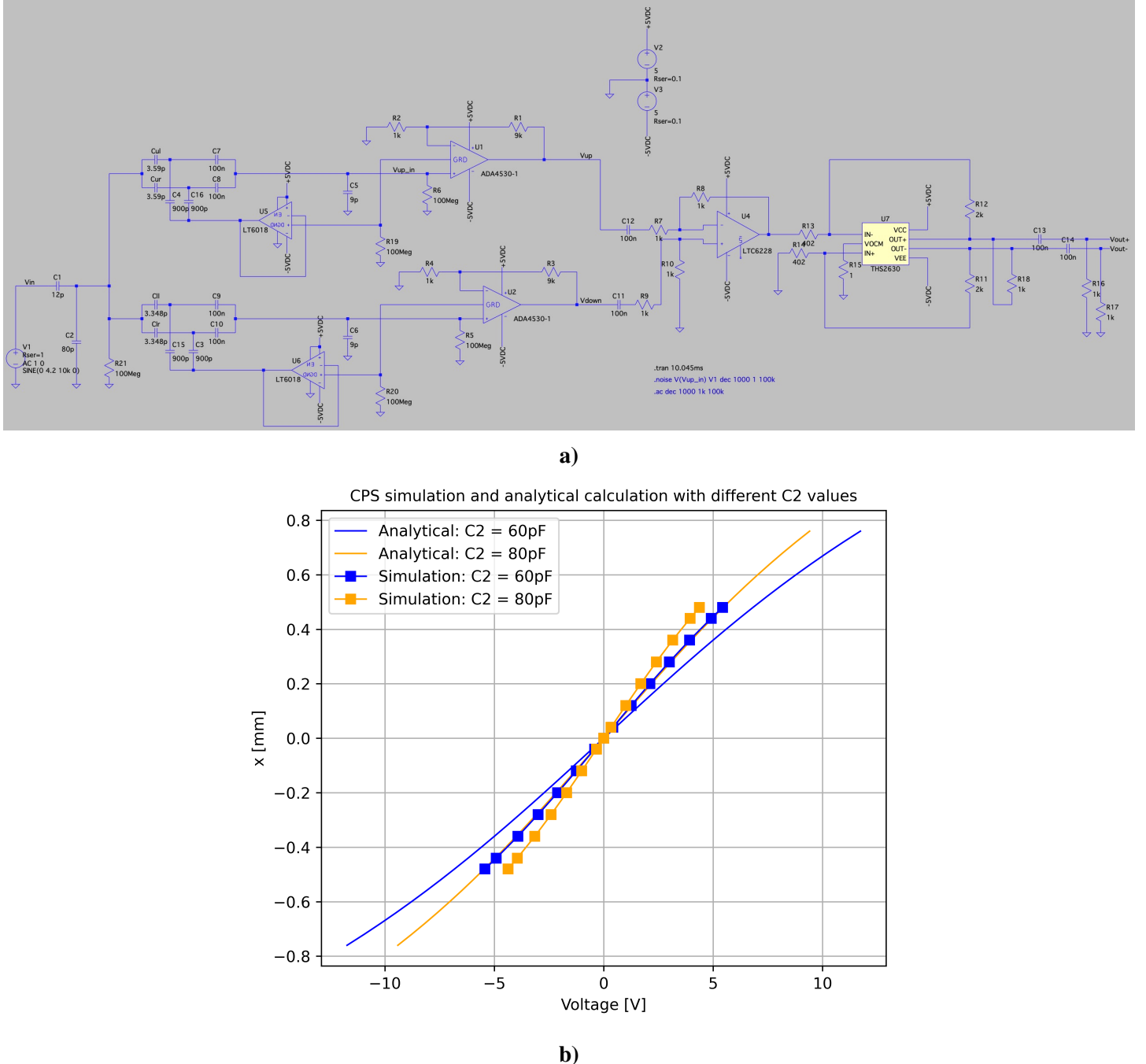


Figure 18: **a)** The circuit schematic of the CPS in *LTspice*. **b)** The comparison of simulation and analytical calculation, with C_2 being a variable. A cubic fit is performed on the analytical transfer function with $C_2 = 60\text{ pF}$. The gain from the simulation is higher than the one from the analytical calculation, showing how the noise from the electronics components influence the transfer function.

the Virgo experiment, under the translation δx which was read from the micrometric screw. The gain was calculated as $\delta x / \delta V$, with particular focus on the region near

3 Displacement Sensors for the End Mass

the centre position of the end mass.

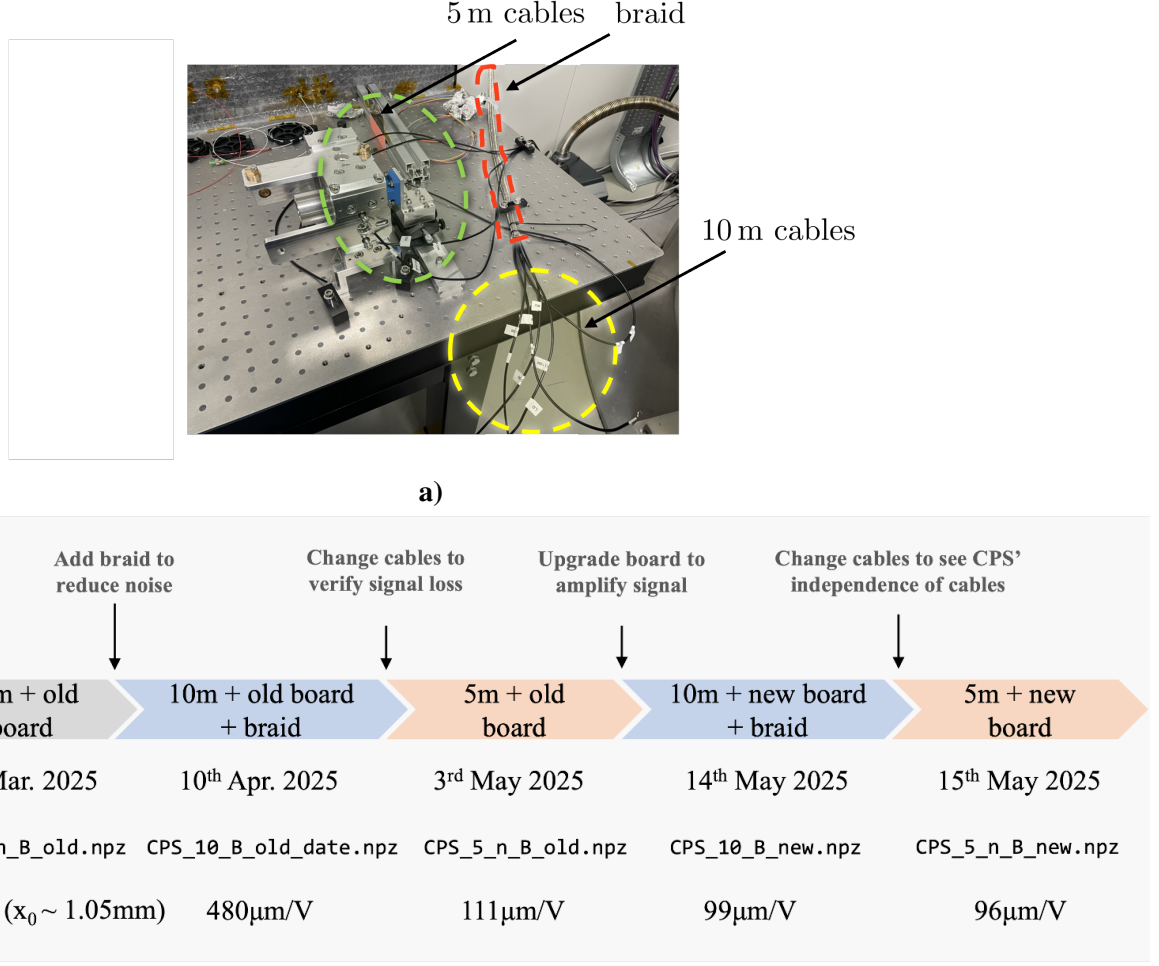


Figure 19: **a)** Setup of the end mass system during the noise testing and upgrade phase. Two cable configurations are shown: 5 m cables without braid (green circle) and 10 m braided cables (yellow circle). **b)** The CPS optimization process, including the action taken, setups, timeline, the name for the stored data, and the gain measured with micrometric screw around the centre position. The noise spectrum for different setups are shown in Figure 20.

To optimize setup for lower noise and a stable gain that is independent of the output cabling, we added an additional braid around the five 10 m cables in the original setup to suppress the noise from the environment also to ground the cable, and electronics board was equipped with extra buffers for compensating the signal loss introduced by the braid. A set of 5 m cables without additional external braid was used to replace the output cables, allowing a comparison of the output performance with different cabling. The overall development process of the CPS is summarized in Figure 19.

Noise spectrum was investigated in two ways. For a short test in the lab, we examined the power spectrum of CPS_1_H_RAW from *dataDisplay*. For a throughout test of the noise floor, we collected 7 hours of data from the CPS_1_H_DEMOD_i channel of a static CPS in air overnight, and processed this power spectrum with the correspondence gains to obtain the displacement noise spectrum. Five different setups were tested in the second way:

1. 10 m cables without braid, using old board.
2. 10 m cables with braid, using old board.
3. 5 m cables without braid, using old board.
4. 10 m cables with braid, using the upgraded board.
5. 5 m cables without braid, using upgraded board.

Situation 4. and 5. will be the ultimate setup options for the CPS, as gain stability is a necessity. Figure 20 compares the noise spectra from different setups. The following conclusions can be drawn:

- When using the same electronics board (setups in 1., 2. and 3., and setups in 4. and 5.) shorter cables produced lower noise.
- For setups using 10 m cables (setups 1., 2. and 4.) adding a braid reduced the environmental noise. However, updating of the board traded this benefit away, resulting into the highest noise floor among all the setups.
- Upgrading the electronics board (setup 1. and 3., and setup 2. and 5.) introduced additional noise. This effect was more significant for 10 m cables with braid than for 5 m cables without braid.

Future optimization can explore potential coupling between the board upgrade and braiding the cabling, such as by adding braid to the 5 m cables. So far, setup 5. with 5 m cables and upgraded board shows the best performance, thus is adopted for the following measurements in Section 3.3.3 and Chapter 4.

3.3.3 Performance Test of the CPS

In the coordination of the sensing frame, the CPS is used to find the centre position, labelled as (x_{H0}, x_{V0}) as shown in Figure 21. This position is calibrated when the end mass is located at (x_{Hs}, x_{Vs}) , where the CPS readout is zero in both horizontal and vertical directions.

Ideally, the geometric centre (x_{H0}, x_{V0}) and the sensing centre (x_{Hs}, x_{Vs}) are overlapped as the same point. However, a small offset might exist, due to manufacture mismatch from the design, or gain differences in the amplifying board. To evaluate this small offset, the sensing centre is determined as the point where the transfer function of voltage to the displacement has the maximum gradient. This is due to the symmetric property of the transfer function, as calculated in 3.15.

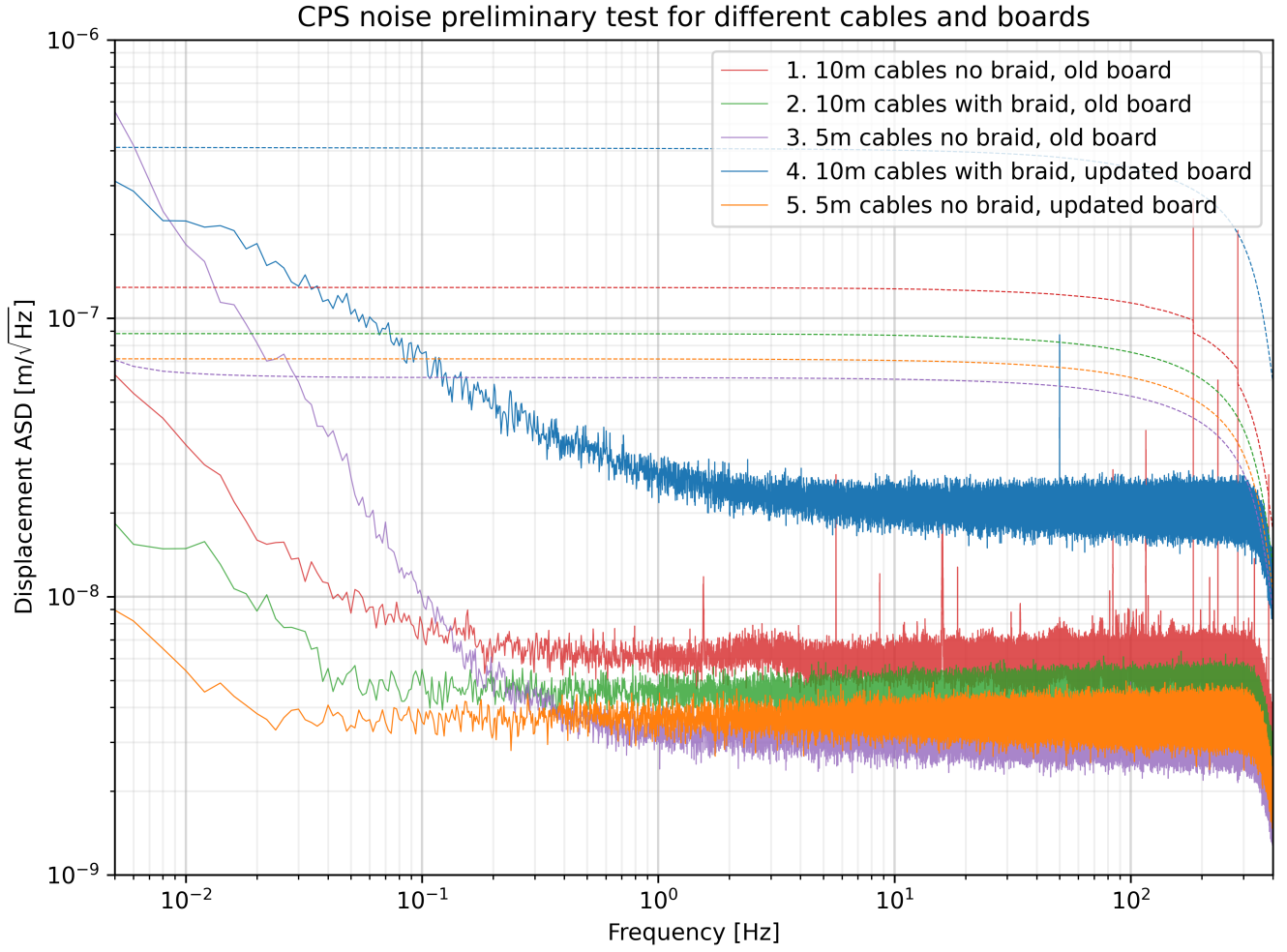


Figure 20: The displacement noise spectrum and the rms of the noise for five CPS setups. The code of this plot can be found in Appendix A.

The cubic fit for the CPS transfer function, calibrated using HoQIs after discarding edge data and scanning from right to left, is:

$$x [\mu\text{m}] = -0.214 [\mu\text{m}/\text{V}^3] V_{\text{CPS}}^3 [\text{V}^3] + 0.032 [\mu\text{m}/\text{V}^2] V_{\text{CPS}}^2 [\text{V}^2] + 92.618 [\mu\text{m}/\text{V}] V_{\text{CPS}} [\text{V}] \quad (3.17)$$

in which the readout of HoQI is calibrated to have $x = 0 \mu\text{m}$ when $V_{\text{CPS}} = 0 \text{ V}$. The extra second order term in the cubic fit indicates that the biggest gradient point wouldn't lie on the $V_{\text{CPS}} = 0 \text{ V}$ axis. $\delta x / \delta V_{\text{CPS}}$ reaches its maximum at $V_{\text{CPS}} = 0.033 \text{ V}$, resulting in an offset of $3.05 \mu\text{m}$ shown in Figure 22, which is negligible for calibrating the centre position.

Thus, comparing the result from the analytical model, simulation and one measurement using HoQIs in Chapter 4. The performance of the CPS from analytical model,

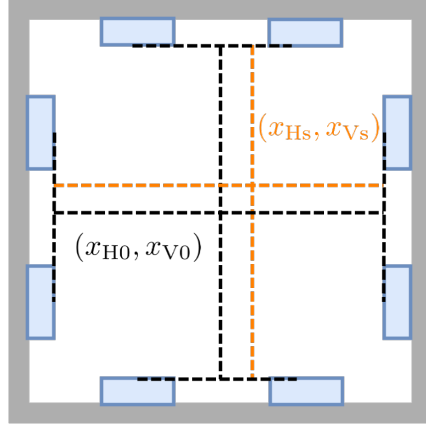


Figure 21: The coordination system within the sensing frame. (x_{H0}, x_{V0}) representing the geometric centre of the end mass system, (x_{H0}) is the location when the CPS readout V_{CPS} is zero in both horizontal and vertical directions.

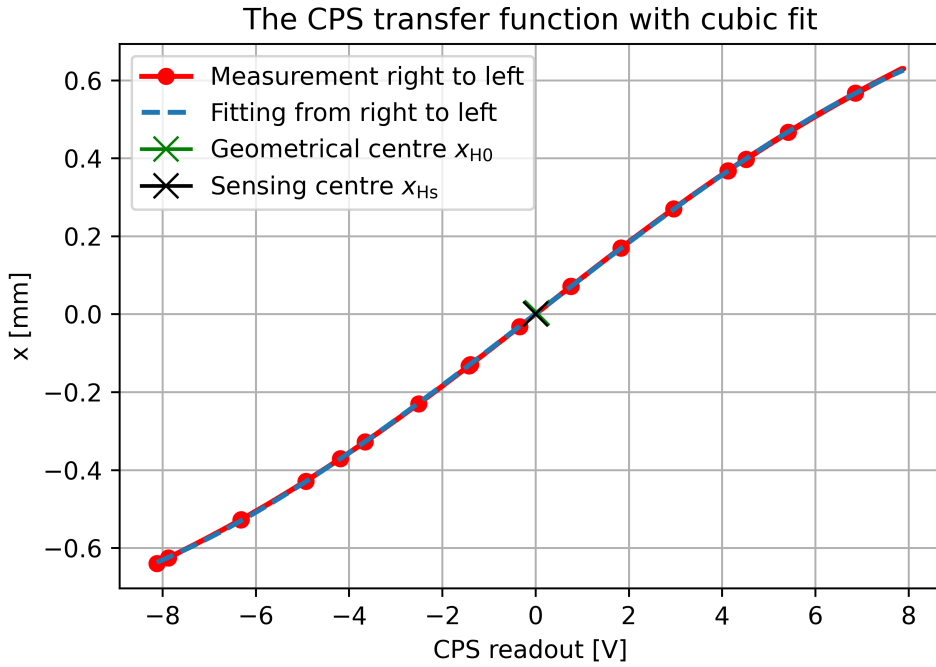


Figure 22: Calibration of the CPS using HoQI, with the end mass scanned from right to left. A cubic fit is applied to determine the point of maximum gradient, with its geometrical centre x_{H0} marked by the green cross on the curve. The sensing centre when $V_{CPS} = 0$ V is marked by the black cross.

simulation and the measurement using HoQIs agree well with each other, within a small uncertainty of capacitance of C_2 , see Figure 23.

Together with the noise analysis in Figure 20 and the independence from output

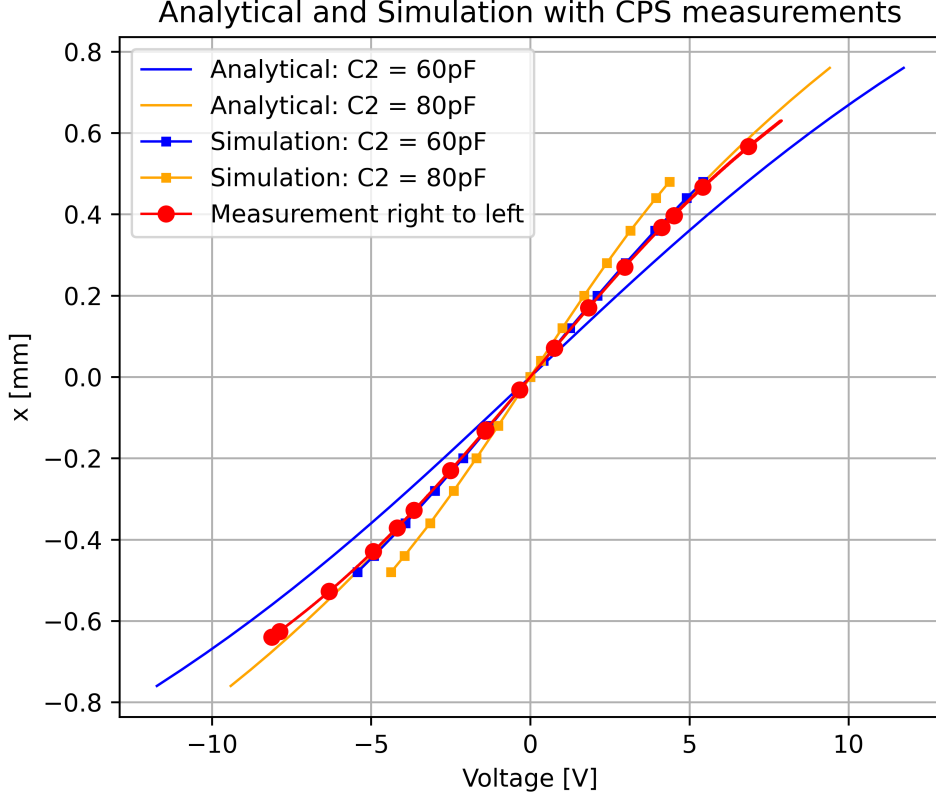


Figure 23: The comparison of the analytical model and the simulation for $C_2 = 60$ pF and $C_2 = 80$ pF, along with the measurement using HoQIs scanning from right to left. Curves with the same colour representing the result using the same C_2 capacitance. In this plot, the best approximation from the analytical model is $C_2 = 80$ pF , and from simulation is $C_2 = 60$ pF.

cabling, we conclude that the CPS developed in this work is a functional, reliable, and low noise wideband sensor with predictable performance.

3.4 The Homodyne Quadrature Interferometer (HoQI)

HoQI is a compact homodyne quadrature interferometer that provides low noise and high dynamic range in displacement sensing, and is used for calibrating the CPS and testing the collaboration of CPS-HoQI sensing system. The sensitivity of HoQI surpasses all of the currently displacement sensors employed on gravitational waves detectors [27]. It is a Mach-Zehnder interferometer with three photodiodes (PDs), enabling simultaneous measurement of both quadratures. From the optical layout illustrated in Figure 24, the optical power at the photodiodes are:

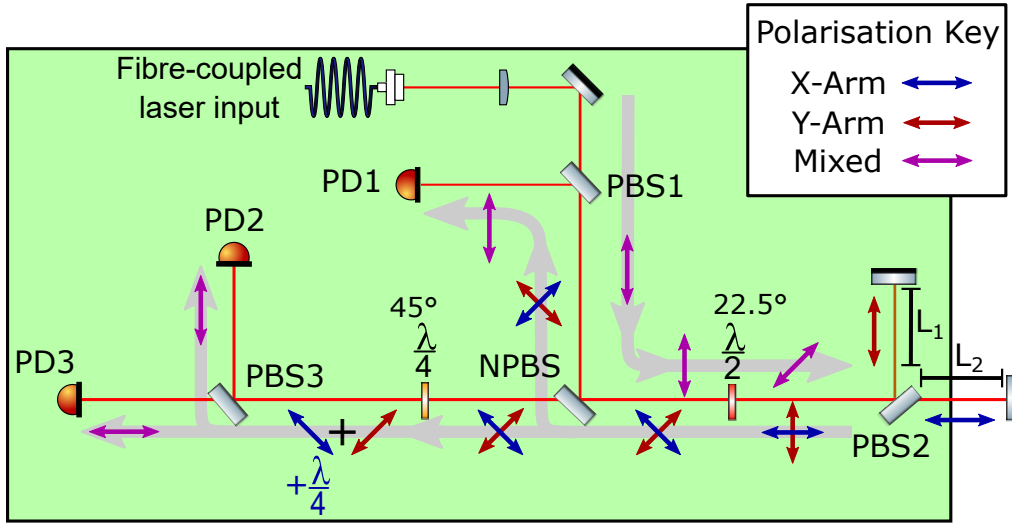


Figure 24: The layout shows the locations of the optical components, as well as the direction and polarization of the laser beam. The HoQIs assembly base plate is pale green block. A collimated beam is injected into a polarising beamsplitter (PBS), producing a linearized laser beam. The reflected beam from a non-polarising beamsplitter (NPBS) is later split into two paths: the reference arm L_1 within the HoQI frame, and the test arm L_2 with one retro reflector mounted on the end mass cube. After the polarization is modified by a half waveplate ($\lambda/2$) and a quarter waveplate ($\lambda/4$), the interfered beam is directed to the three photodiodes (PDs).

$$\begin{aligned} P_{\text{PD1}} &= \frac{P_{\text{in}}}{8} (1 + a \sin(\phi)) \\ P_{\text{PD2}} &= \frac{P_{\text{in}}}{8} (1 - a \cos(\phi)) \\ P_{\text{PD3}} &= \frac{P_{\text{in}}}{8} (1 + a \cos(\phi)) \end{aligned} \quad (3.18)$$

where P_{in} is the input power from the collimated beam, $\phi = \frac{4\pi}{\lambda}(L_1 - L_2)$ shows phase mismatch due to the difference length of the light path from two arms, and a is the fringe visibility. Thus, the quadrature information of the interference is:

$$\begin{aligned} Y &\propto P_{\text{PD1}} - P_{\text{PD2}} = \frac{\sqrt{2}aP_{\text{in}}}{8} \sin\left(\phi + \frac{\pi}{4}\right) \\ X &\propto P_{\text{PD1}} - P_{\text{PD3}} = \frac{\sqrt{2}aP_{\text{in}}}{8} \sin\left(\phi - \frac{\pi}{4}\right) \\ \arctan\left(\frac{Y}{X}\right) &\propto \phi = \frac{4\pi}{\lambda}(L_1 - L_2) \end{aligned} \quad (3.19)$$

In this experiment we assembled and calibrated some HoQIs for the full future oper-

ation of OmniSens. To prepare a HoQI, the optical components were either glued or screwed onto the base plate. The collimator was adjusted to ensure reflected beams from two arms overlap around the centre of PDs. Once aligned, HoQI was mounted on the end mass sensing frame, as shown in the front view in Figure 10. a). Two cams allowed HoQI to move freely along the two-dimensional frame surface of the frame to maximize the fringe visibility on PDs.

In this experiment, the fringe visibility of PD1, which corresponds to the sin signal, was suppressed probably due to the scattered light reflecting from the base plate structure. An ellipse fitting was performed to eliminate the non-linear effects in the X and Y signal defined in 3.19. Figure 25 presents the unwrapped Lissajous figure of X and Y when the end mass cube moves at a speed below $v_{\max} = \lambda f_{\text{sampling}}/8 \approx 25 \text{ mm/s}$.

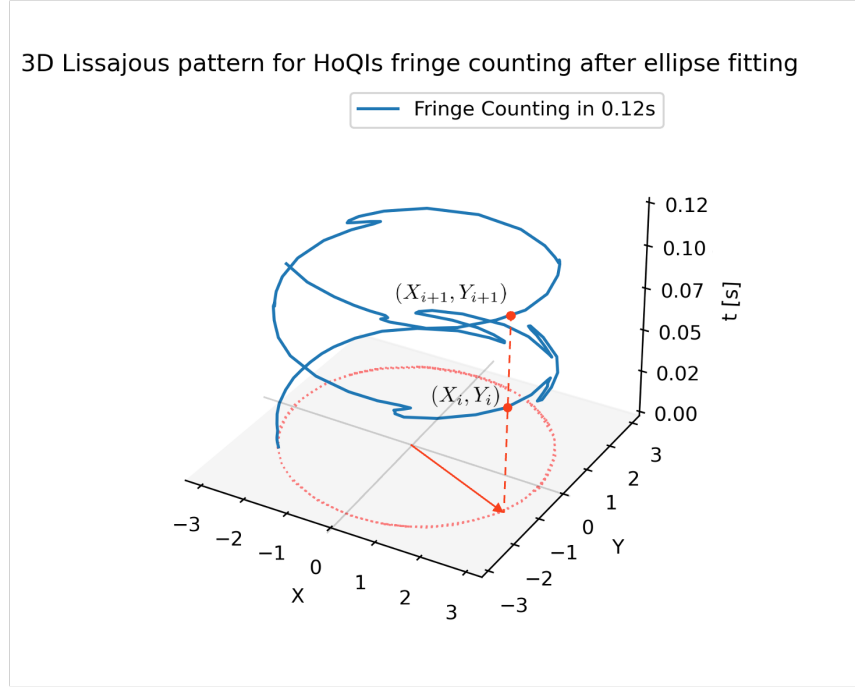


Figure 25: Unwrapped Lissajous figure of X and Y with the test arm mirror slowing moving. X - Y plane represents the phase space. A good ellipse fitting calibrates (X, Y) to lie on a circle centred at $(0, 0)$, with $\arctan(Y/X) \propto (L_1 - L_2)$. Using the unwrapping algorithm, $L_1 - L_2$ can be continuously tracked through fringe counting. When (X_i, Y_i) and (X_{i+1}, Y_{i+1}) are sitting on the adjacent fringes and have the same projection on the X - Y plane, the test arm mirror travels for a distance of $\lambda/2$.

From the static in-vacuum test of the upgraded HoQIs, a peak sensitivity of $2.5 \times 10^{-14} \text{ m}/\sqrt{\text{Hz}}$ at 100 Hz, and $2.3 \times 10^{-12} \text{ m}/\sqrt{\text{Hz}}$ at 10 mHz was achieved [10].

4 Results

The experimental work in this master's project aims to validate strategy of using the CPS and HoQI to find the absolute position of the end mass within the sensing frame, as described in Section 2.2.

In this masters project, the CPS–HoQI sensing scheme was tested in a round-trip across the full horizontal dynamic range of the end mass. CPS were calibrated using HoQI with higher resolution, cubic fittings were determined. This chapter analyses the scanning data to identify functional conditions and potential malfunction mechanisms. The benefit of such a displacement sensing system and indications for future OmniSens operation are discussed.

4.1 Calibrating the CPS with HoQI

Two one-to-one relationships between the horizontal CPS and HoQI readouts were obtained by a step moving approach in a round-trip scan across the full horizontal dynamic in 3660 s. The micrometric screw firstly moved the end mass from the left end to the right end in the first 680 s, then the end mass was positioned around the centre, finally starting from 2580 s, the end mass scanned from the right end to the left end. Each step spanning around 0.1 mm and staying for 45 s, as demonstrated in Figure 27.

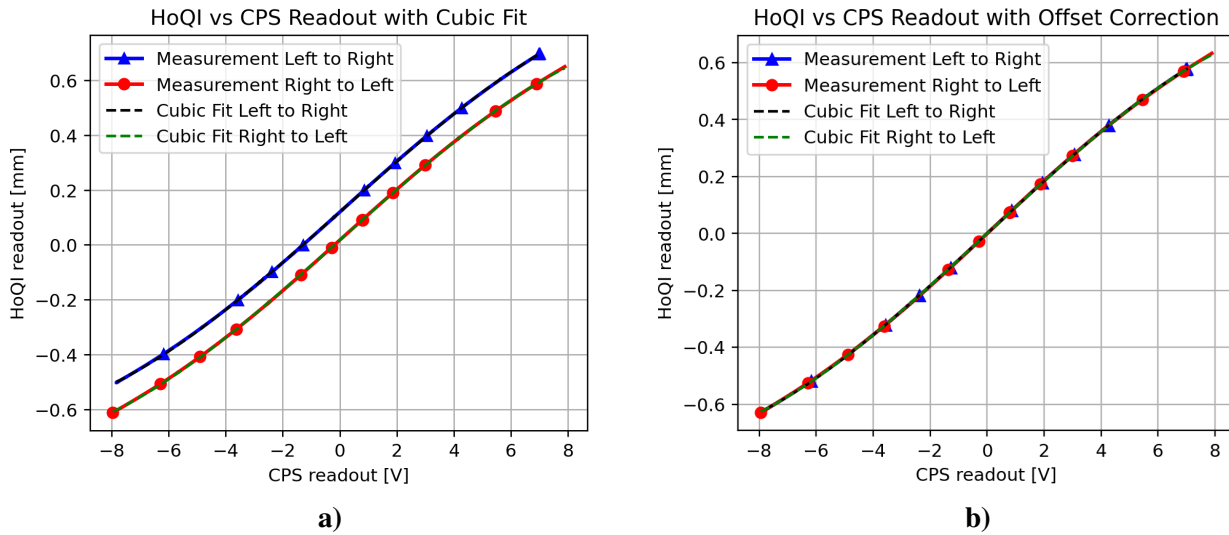


Figure 26: **a)** The scanning readout for two directions and their cubic fits, truncated the data around limited position of the end mass.
b) Measurements and cubic fits with offset correction.

After discarding the edge data to exclude short cut behaviour, a cubic fit was applied to the scanning result. Figure 26.a) shows the measurement and the fitting in CPS calibration. The cubic fitted the transfer functions are:

4 Results

$$\begin{aligned} \text{Left to right: } x [\mu\text{m}] = & -0.217 [\mu\text{m}/\text{V}^3] V_{\text{CPS}}^3 [\text{V}^3] + 0.038 [\mu\text{m}/\text{V}^2] V_{\text{CPS}}^2 \\ & + 92.745 [\mu\text{m}/\text{V}] V_{\text{CPS}} [\text{V}] + 119.397 [\mu\text{m}] \end{aligned}$$

$$\begin{aligned} \text{Left to right: } x [\mu\text{m}] = & -0.214 [\mu\text{m}/\text{V}^3] V_{\text{CPS}}^3 [\text{V}^3] + 0.032 [\mu\text{m}/\text{V}^2] V_{\text{CPS}}^2 \\ & + 92.618 [\mu\text{m}/\text{V}] V_{\text{CPS}} [\text{V}] + 17.305 [\mu\text{m}] \end{aligned}$$

The fitted transfer functions show that between the two scanning processes the offset between the HoQI and the CPS data differs by 0.112 mm. From Figure 26.b), after the offset correction and calibrated the HoQI's readout as $x = 0$ mm when $V_{\text{CPS}} = 0$ V, two measurements curves and their cubic fits overlap with each other. Since the CPS is an absolute sensor with transfer function only related to the mechanical and electronical setups which wasn't changed during the scanning process, whereas HoQI can only be sensitive to the relative displacement, we firstly assumed the 0.112 mm offset was mainly coming from a shift in HoQI's readout.

4.2 Offset Analysis

Using the same cubic fit, the whole scanning process is reproduced in Figure 27, with the cubic fit for the CPS and an offset correction for HoQI. The readout from two sensors matched each other except for operating near the edge of the moving range which can be located the short cut behaviour. From the X and Y channel plot, we see the fringe visibility maintained at the same level for the most of the time.

From the accumulated offset during scanning (middle plot in Figure 27), a net offset of 0.112 mm appeared when the end mass was at the right edge (500–1000 s). This discrepancy cancelled out when the end mass moved to the right edge and returned (2250–2570 s).

In time intervals where CPS and HoQI recorded identical displacements, the sensing system performed exactly as we expected, validating the effectiveness of the CPS-HoQI sensing scheme. For example between 60.90 s and 61.10 s in Figure 28, the CPS and HoQI readouts overlapped. HoQI's curve appeared to be much smoother due to its lower noise floor, whereas the CPS traced more fluctuations. The sin and cos signal, along with the Lissajous pattern, were all continuos and smooth, confirming that no fringe slipping occurred in this duration.

On the contrary, the measurement between 846.50 s and 847.00 s in Figure 29 captured the very 0.1 mm offset of the HoQI with a clear fringe slipping behaviour. The moving speed of the end mass during this time was 3 mm/s which is slower than the maximum speed, ruling out the possibility of down sampling. The phase and the fringe counting were lost during a time period that was longer than offset was accumulating, indicating a possible temporary loss of the interference.

Another information can be derived from Figure 27. The CPS readout implied an entire sensing range of 1.35 mm with the cubic fit, whereas HoQI readout covered up to 1.46 mm, and the micrometric screw measurement recorded 1.48 mm in Table 1. Given a stable input power, HoQI can only record displacements smaller than the

4 Results

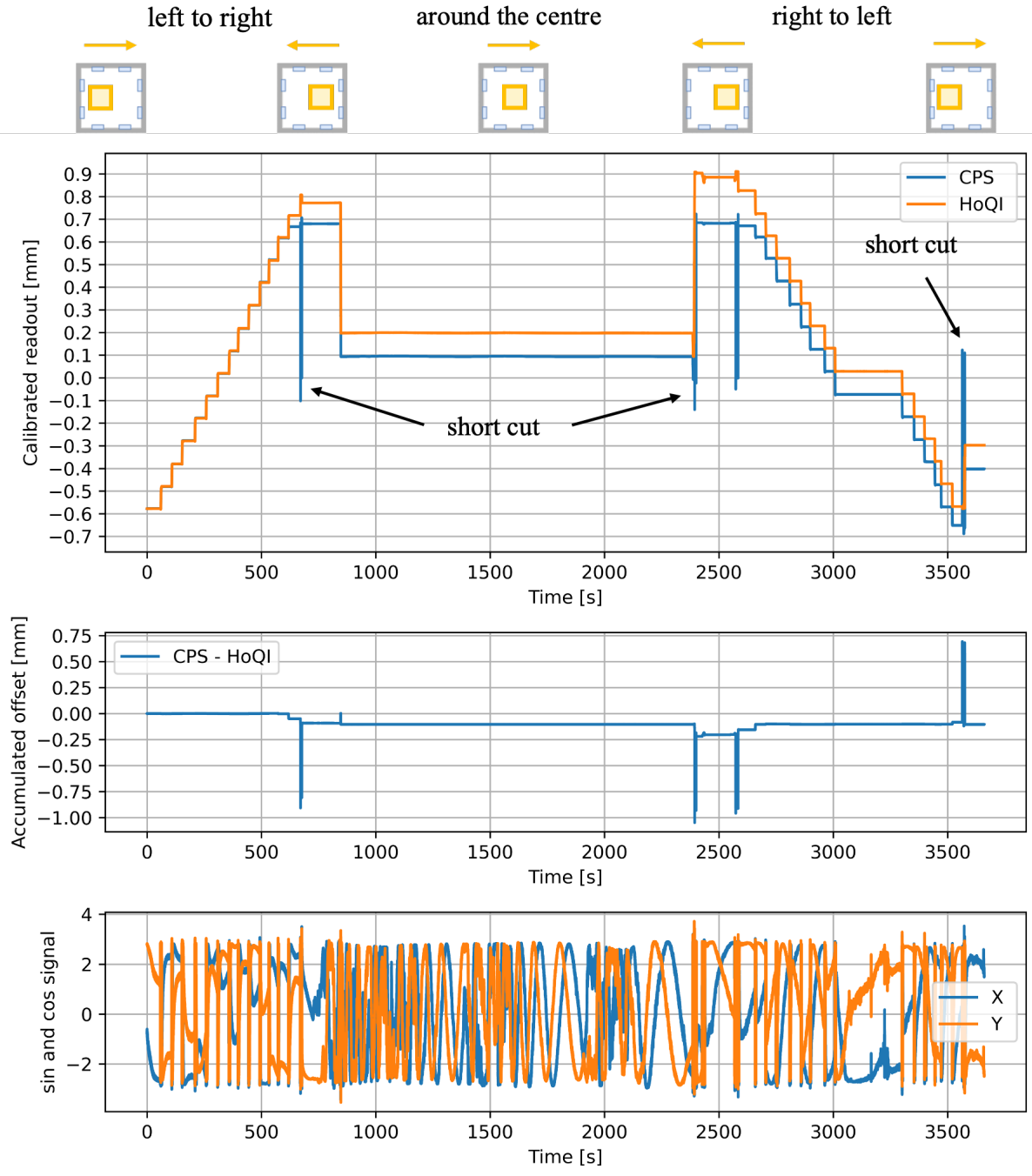


Figure 27: The round-trip scanning experiment in time domain. On the top illustrates the movement and the location of the end mass along with time. Cubic fitted CPS data and the HoQI data after offset calibration are shown together with their accumulated discrepancy. At the bottom shows the X and Y channel representing the sin and cos signal of the interfered light.

actual travel distance in a single-direction movement. This implies that the cubic fit

4 Results

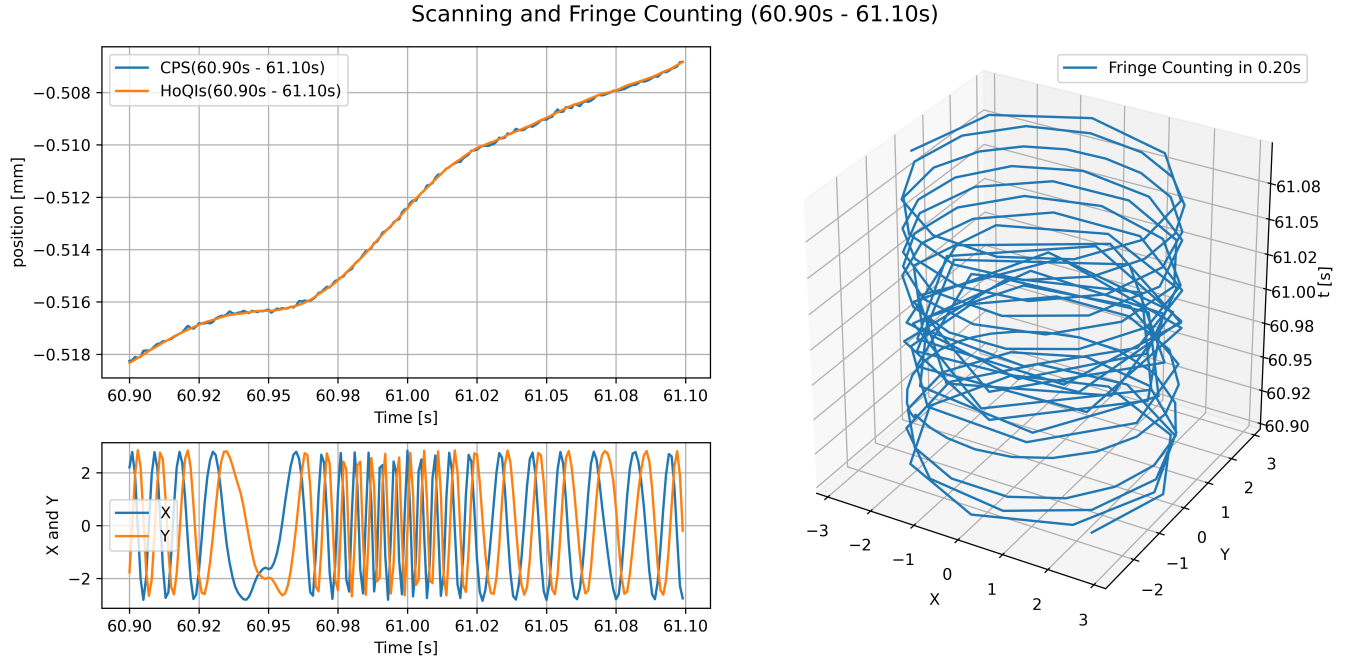


Figure 28: CPS and HoQI readouts comparison and the Lissajous pattern between 60.90 s and 61.10 s.

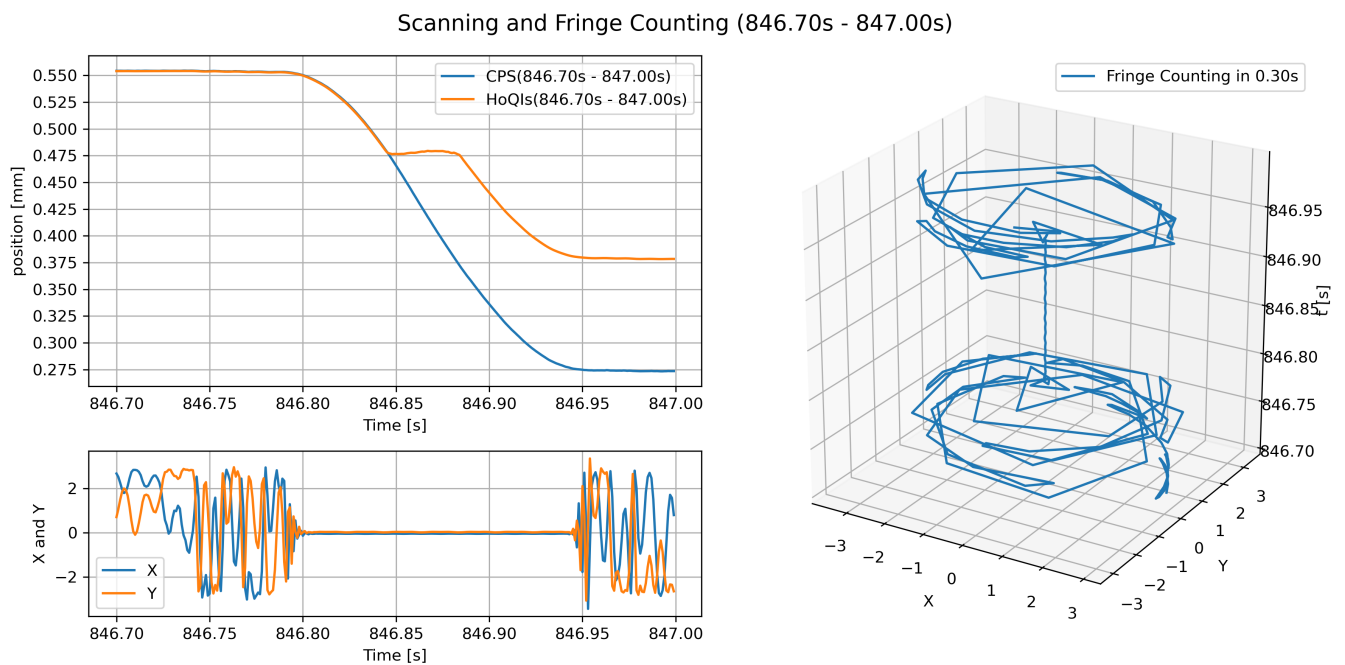


Figure 29: CPS and HoQI readouts comparison and the Lissajous pattern between 846.50 s and 847.00 s.

4 Results

of the CPS reproduces a range smaller than the true dynamic range. As discussed in Section 3.3.3, the analytical model, simulation, and measurements agree well within the region excluding the moving edge. It is therefore natural to examine the CPS behaviour when the circuit approaches a short-circuit condition. For this purpose, the time interval from 2584 s to 3564 s is selected for further analysis.

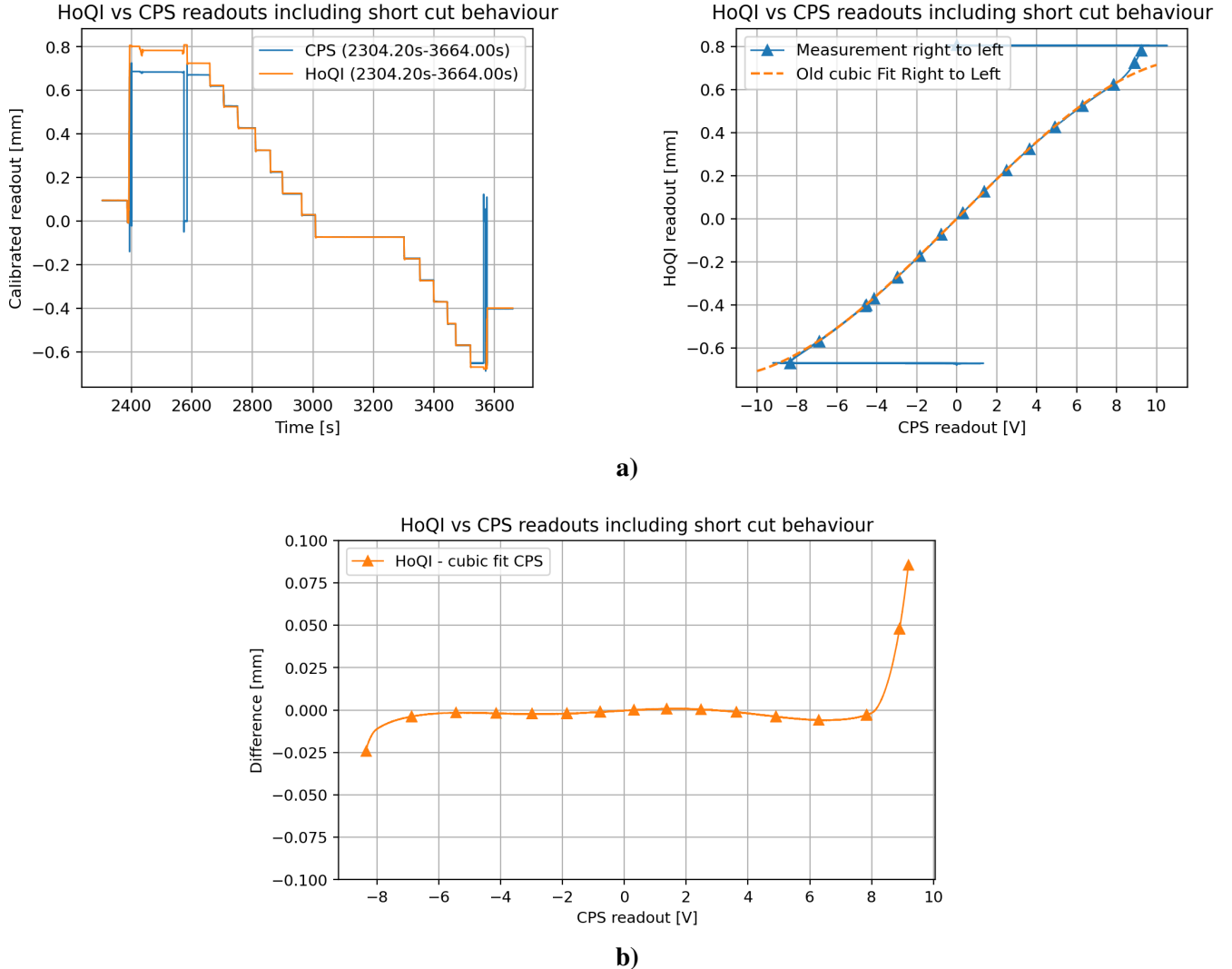


Figure 30: a) A comparison of the HoQI readout and the cubic fitted CPS readout. b) The difference between the HoQI readout and the cubic fitted CPS readout at different CPS readout.

Figure 30 compares the original cubic fit with the calibration data. While the cubic fit aligned well with the measurement overall, at the near short-circuit position the same displacement produced a smaller change in measured voltage than predicted by the fit. This indicates that the actual gain of the transfer function is higher than that of the fitted model as the end mass approaches the edge, and that the cubic fit no longer accurately represents the CPS voltage-to-position transfer function in this

4 Results

region.

As discussed in Section 3.3.1, the stray capacitance C_2 influences the transfer function such that an increase in C_2 leads to a higher gain. When the end mass moved toward the metal stop on one side, C_2 may effectively increase due to the distance to the sensing frame got smaller, resulting in a higher gain than if C_2 was assumed to be a constant. This hypothesis also explains why during the period from 2380 s to 2600 s, the end mass travelled to the right edge and returned without any accumulated offset.

5 Conclusion

In this master’s thesis, a Capacity Position Sensor (CPS) tailored for OmniSens was designed and constructed from scratch. The analytical model, electronic simulations, and the experimental measurements of the CPS agree well with each other. Functional testing demonstrates that the CPS is a reliable sensor, with a stable response to the position independent of the cabling. The optimized setup achieves a noise floor of $7 \times 10^{-8} \text{ m}/\sqrt{\text{Hz}}$ at 0.1 Hz.

A one-dimensional translation test of the end mass position sensing system, a combination from the CPS and HoQI, confirms that the CPS is effective for locating the centre position, while the HoQIs significantly enhance displacement sensitivity. As long as HoQIs guarantee to provide a precise inertial movement measurement of the active platform, the CPS-HoQI combination can enable maintaining OmniSens to the designed working position through a robust control scheme. This also enables OmniSens to establish and hold a new working point when necessary, for example, if a change in buoyancy disrupts the balance of the reference mass and a new equilibrium must be found.

Potential malfunction scenarios were also identified, such as the offsets discussed in Section 4.2. Offsets are not the primary concern, as the design of OmniSens ensures a small dynamic range around the centre position. All observed offsets during scanning occurred near the travel limits. The CPS-HoQI sensing system can resolve such anomalies effectively: the CPS, as an absolute position sensor, can be used to verify fringe slipping of HoQI, while the low coupling of HoQI to the surrounding structure can help with commissioning the CPS.

Future work on the CPS-HoQI end mass position sensing system can explore its performance across more degrees of freedom, including rotation sensing, determining the maximum translation range of the end mass for the HoQI on the perpendicular axis to maintain interference, and measuring the end mass translation along the arm.

Acknowledgements

I wish to express my heartfelt gratitude to everyone who has supported me during my master's studies, knowing that words can never be enough. Without you, I could not have imagined coming this far.

It has been an extraordinary year working with one of the most outstanding teams in gravitational wave research. My supervisor, Conor, and my daily supervisor, Michele, have done an excellent job in guiding me into this field of instrumental research, something that I had no prior knowledge of. Looking back, I am deeply thankful for their patience and dedication in helping me understand concepts that were, at first, completely counter-intuitive. Sometimes it's funny that, while in the shower or biking somewhere, I would suddenly realise the meaning of something they had explained two weeks earlier.

Under their guidance, and with the invaluable help of our beloved electronics technician Tim, Hans and Gino, mechanical engineer Armin, and Dr.Darling Alex, I have had the joy of getting hands-on experience and receiving thorough training in electronics, optics, and engineering within the OmniSens project. Martin, I have heard much about your excellence as a researcher and supervisor; although we have spoken only briefly, I look forward to working with or discussing ideas with you in the future.

The diverse research topics pursued in the Nikhef gravitational-wave group have kept me connected to the broader dynamics of gravitational-wave research and its social and industrial impact. Even in difficult years, I have witnessed the inspiring story of people striving to make the best of their world. Nikhef will forever be my favourite place to imagine myself doing research: a safe, welcoming environment with a vintage charm that reminds me of the golden age of physics in the last century.

I have found family-like support here, which has been one of the greatest factors in my growth. Alina, Yashwant, Emma, Suzanne, and all the noisy Gen Z younglings, you have been my partners in being joyfully crazy without worry. I have loved the atmosphere of having people willing to do something purely for fun (and sometimes, wonderfully, for no good reason at all). I also cherish the vibrant environment and the life-enjoying philosophy of the Mechanical and Electronics Department. Thank you, Daniel, Nico, Ama, and Cynthia, for all the reassuring conversations. Special thanks to Jop, who has supported me for the past three years, sharing both laughter and tears, and helping me find my place in this foreign land and along this new life path.

Words can never fully capture how I feel upon finally making it through. I wish all the best to the people I love, and to the world we care for, even if all I can offer is my faintest effort.

寄蜉蝣于天地，渺沧海之一粟。

We are like mayflies wandering in this terrestrial world or a grain of millet drifting on a deep ocean.

— 苏轼 《前赤壁赋》

— Su Shi “Former Ode on the Red Cliffs”

林兆青

11.08.2025

References

- [1] B. P. Abbott et al. “Observation of Gravitational Waves from a Binary Black Hole Merger”. In: *Phys. Rev. Lett.* 116 (6 02/2016), p. 061102. DOI: [10.1103/PhysRevLett.116.061102](https://doi.org/10.1103/PhysRevLett.116.061102). URL: <https://link.aps.org/doi/10.1103/PhysRevLett.116.061102>.
- [2] A. Einstein and N. Calder. *Relativity: The Special and General Theory*. Penguin Classics, 2006.
- [3] LIGO Laboratory. *Sources and Types of Gravitational Waves*. Accessed: 2025-08-10. URL: <https://www.ligo.caltech.edu/page/gw-sources>.
- [4] Christopher Moore, Robert Cole, and Christopher Berry. *Gravitational Wave Sensitivity Curve Plotter*. <http://gwplotter.com/>. Accessed: 2025-08-10. 2014.
- [5] Shanika Galaudage. *Science infographics*. 03/2024. URL: <https://photos.google.com/share/AF1QipP-dHXamnGtn1SzCHqe9cfpzFuSLv56J60XKiQGRNK5gRsM4qQtqsEKjnR0nbtXRA?key=ZTJIUTZxMm1UME1SVVNxUHJiQTVwSDVnd1dFa0VB> (visited on 03/18/2024).
- [6] Albert Einstein. “Über Gravitationswellen”. In: *Sitzungsber. Preuss. Akad. Wiss. Berlin (Math. Phys.)* 1918 (1918), pp. 154–167.
- [7] Peter S. Shawhan. “Gravitational Waves and the Effort to Detect Them”. In: *American Scientist* 92.4 (2004), pp. 350–357. DOI: [10.1511/2004.4.350](https://doi.org/10.1511/2004.4.350). URL: <https://www.americanscientist.org/article/gravitational-waves-and-the-effort-to-detect-them>.
- [8] Charlotte Bond et al. “Interferometer techniques for gravitational-wave detection”. en. In: *Living Reviews in Relativity* 19.1 (12/2016), p. 3. ISSN: 2367-3613, 1433-8351. DOI: [10.1007/s41114-016-0002-8](https://doi.org/10.1007/s41114-016-0002-8). URL: <http://link.springer.com/10.1007/s41114-016-0002-8> (visited on 11/11/2024).
- [9] M. Bailes et al. “Gravitational-wave physics and astronomy in the 2020s and 2030s”. In: *Nature Reviews Physics* 3.5 (05/2021), pp. 344–366. ISSN: 2522-5820. DOI: [10.1038/s42254-021-00303-8](https://doi.org/10.1038/s42254-021-00303-8). URL: <https://doi.org/10.1038/s42254-021-00303-8>.
- [10] A. L. Mitchell. “HoQI - Low-noise Interferometric Sensors for the Future of Gravitational Wave Detectors”. English. PhD-Thesis - Research and graduation internal. Vrije Universiteit Amsterdam, 03/2025. DOI: [10.5463/thesis.1032](https://doi.org/10.5463/thesis.1032).
- [11] LIGO Instrument Science List et al. “Sensitivity and Performance of the Advanced LIGO Detectors in the Third Observing Run”. In: *Physical Review D* 102.6 (09/2020). arXiv:2008.01301 [astro-ph], p. 062003. ISSN: 2470-0010, 2470-0029. DOI: [10.1103/PhysRevD.102.062003](https://doi.org/10.1103/PhysRevD.102.062003). URL: [http://arxiv.org/abs/2008.01301](https://arxiv.org/abs/2008.01301) (visited on 07/03/2025).

- [12] Hang Yu et al. “Prospects for Detecting Gravitational Waves at 5 Hz with Ground-Based Detectors”. In: *Phys. Rev. Lett.* 120 (14 04/2018), p. 141102. DOI: [10.1103/PhysRevLett.120.141102](https://doi.org/10.1103/PhysRevLett.120.141102). URL: <https://link.aps.org/doi/10.1103/PhysRevLett.120.141102>.
- [13] B. S. Sathyaprakash and Bernard F. Schutz. “Physics, Astrophysics and Cosmology with Gravitational Waves”. en. In: *Living Reviews in Relativity* 12.1 (12/2009), p. 2. ISSN: 2367-3613, 1433-8351. DOI: [10.12942/lrr-2009-2](https://doi.org/10.12942/lrr-2009-2). URL: <http://link.springer.com/10.12942/lrr-2009-2> (visited on 06/21/2025).
- [14] ET Steeting Committee Editorial Team. “ET design report update 2020”. In: *ET Documents* (09/2020). URL: <https://apps.et-gw.eu/tds/?content=3&r=16984>.
- [15] Teng Zhang, Stefan Danilishin, and Mikhail Korobko. “Instrument Science for the Einstein Telescope”. In: *ET Collaboration Report* (07/2025). URL: <https://www.overleaf.com/read/qjrcqmyvhk>.
- [16] Michele Maggiore et al. “Science case for the Einstein telescope”. In: *Journal of Cosmology and Astroparticle Physics* 2020.03 (03/2020), p. 050. ISSN: 1475-7516. DOI: [10.1088/1475-7516/2020/03/050](https://doi.org/10.1088/1475-7516/2020/03/050). URL: <https://dx.doi.org/10.1088/1475-7516/2020/03/050>.
- [17] C. M. Mow-Lowry and D. Martynov. “A 6D interferometric inertial isolation system”. In: *Classical and Quantum Gravity* 36.24 (11/2019). Publisher: IOP Publishing, p. 245006. DOI: [10.1088/1361-6382/ab4e01](https://doi.org/10.1088/1361-6382/ab4e01). URL: <https://dx.doi.org/10.1088/1361-6382/ab4e01>.
- [18] Fabrice Matichard and Matthew Evans. “Review: Tilt-Free Low-Noise Seismometry”. en. In: *Bulletin of the Seismological Society of America* 105.2A (04/2015). Publisher: Seismological Society of America (SSA), pp. 497–510. ISSN: 0037-1106, 1943-3573. DOI: [10.1785/0120140200](https://doi.org/10.1785/0120140200). URL: <https://pubs.geoscienceworld.org/bssa/article/105/2A/497-510/331837> (visited on 07/15/2025).
- [19] Walter Fichter et al. “LISA Pathfinder drag-free control and system implications”. In: *Classical and Quantum Gravity* 22.10 (05/2005). Publisher: IOP Publishing, S139–S148. ISSN: 0264-9381, 1361-6382. DOI: [10.1088/0264-9381/22/10/002](https://doi.org/10.1088/0264-9381/22/10/002). URL: <https://iopscience.iop.org/article/10.1088/0264-9381/22/10/002> (visited on 07/14/2025).
- [20] S. J. Cooper et al. “Sensors and actuators for the advanced LIGO A+ upgrade”. In: *Review of Scientific Instruments* 94.1 (01/2023), p. 014502. ISSN: 0034-6748. DOI: [10.1063/5.0117605](https://doi.org/10.1063/5.0117605). URL: <https://doi.org/10.1063/5.0117605> (visited on 08/05/2025).
- [21] Virgo Collaboration. *PythonVirgoTools*. <https://git.ligo.org/virgo/virgoapp/PythonVirgoTools>.
- [22] The International Gravitational-Wave Observatory Network. *GWpy*. <https://gwpy.github.io/>. Version 3.0.13.

- [23] J. Casanueva. “Acl for commissioners”. In: *Virgo Documents* (09/2019). URL: <https://tds.virgo-gw.eu/?r=16177>.
- [24] Nicolas Letendre et al. “Preliminary DaqBox Specifications”. In: *Virgo Documents* (03/2012). URL: <https://tds.virgo-gw.eu/?r=9292> (visited on 03/08/2024).
- [25] V. Josselin, P. Touboul, and R. Kielbasa. “Capacitive detection scheme for space accelerometers applications”. In: *Sensors and Actuators A: Physical* 78.2 (1999), pp. 92–98. ISSN: 0924-4247. DOI: [10.1016/S0924-4247\(99\)00227-7](https://doi.org/10.1016/S0924-4247(99)00227-7). URL: <https://www.sciencedirect.com/science/article/pii/S0924424799002277>.
- [26] D. Verkindt. *Virgo dataDisplay: A software for signal processing and data visualization*. <https://lappweb.in2p3.fr/virgo/dataDisplay/>.
- [27] S J Cooper et al. “A compact, large-range interferometer for precision measurement and inertial sensing”. In: *Classical and Quantum Gravity* 35.9 (03/2018). Publisher: IOP Publishing, p. 095007. DOI: [10.1088/1361-6382/aab2e9](https://doi.org/10.1088/1361-6382/aab2e9). URL: <https://dx.doi.org/10.1088/1361-6382/aab2e9>.

A

```
## get interactive plot
%matplotlib widget

import numpy as np
from matplotlib import pyplot as plt
from matplotlib.ticker import LogLocator
## for plotting ASD
from scipy import signal as sig

CPS_5_10 = np.load("CPS_5_and_10.npz", allow_pickle = True)

I_10_n_B_old = CPS_5_10['I_10_n_B_old'][()]      # setup 1: 10m cables
↪ without braid with old board
I_10_B_old = CPS_5_10['I_10_B_old'][()]          # setup 2: 10m cables with
↪ braid with old board
I_5_n_B_old = CPS_5_10['I_5_n_B_old'][()]          # setup 3: 5m cables
↪ without braid with old board
I_10_B_new = CPS_5_10['I_10_B_new'][()]          # setup 4: 10m cables with
↪ braid with updated board
I_5_n_B_new = CPS_5_10['I_5_n_B_new'][()]          # setup 5: 5m cables
↪ without braid with updated board

def rmsnator(f2, Pxx, fmin=0, fmax=1e10):
    df = f2[1] - f2[0]
    f_selection = (f2>=fmin) & (f2< fmax)
    P_sel = Pxx[f_selection]
    return (f2[f_selection], df * np.cumsum(P_sel[::-1])[::-1])

# In a total data collecting time of 21600s
freq = len(I_10_B_new)/21600
time_window = 500

# Power spectrum
f, P1 = sig.welch(I_10_n_B_old, fs = freq, window = 'hann', nperseg =
↪ time_window * freq, noverlap = time_window * freq // 2, detrend =
↪ 'linear', average = 'median' )
f, P2 = sig.welch(I_10_B_old, fs = freq, window = 'hann', nperseg =
↪ time_window * freq, noverlap = time_window * freq // 2, detrend =
↪ 'linear', average = 'median' )
f, P3 = sig.welch(I_5_n_B_old, fs = freq, window = 'hann', nperseg =
↪ time_window * freq, noverlap = time_window * freq // 2, detrend =
↪ 'linear', average = 'median' )
f, P4 = sig.welch(I_10_B_new, fs = freq, window = 'hann', nperseg =
↪ time_window * freq, noverlap = time_window * freq // 2, detrend =
↪ 'linear', average = 'median' )
f, P5 = sig.welch(I_5_n_B_new, fs = freq, window = 'hann', nperseg =
↪ time_window * freq, noverlap = time_window * freq // 2, detrend =
↪ 'linear', average = 'median' )
```

```

g1 = 188 # I_10_n_B_old
g2 = 480 # I_10_B_old
g3 = 99 # I_5_n_B_old
g4 = 99 # I_10_B_new
g5 = 96 # I_5_n_B_new

# Plotting parameters
linewidth = 0.5
linewidth_2 = 0.5
a=0.8

fig_1, ax = plt.subplots(1,1, figsize=(8,6), dpi = 300)

l1 = ax.loglog(f,np.sqrt(P1)*g1/1e6, linewidth = linewidth_2, label='1. 10m
    ↵ cables no braid, old board', color='C3', alpha=a )
l2 = ax.loglog(f,np.sqrt(P2)*g2/1e6, linewidth = linewidth_2, label='2. 10m
    ↵ cables with braid, old board', color='C2', alpha=a )
l3 = ax.loglog(f,np.sqrt(P3)*g3/1e6, linewidth = linewidth_2, label='3. 5m
    ↵ cables no braid, old board', color='C4', alpha=a)
l4 = ax.loglog(f,np.sqrt(P4)*g4/1e6, linewidth = linewidth, label='4. 10m
    ↵ cables with braid, updated board', color='C0')
l5 = ax.loglog(f,np.sqrt(P5)*g5/1e6, linewidth = linewidth, label='5. 5m
    ↵ cables no braid, updated board', color='C1')

# Calibration
f_rms, P1_rms = rmsnator(f, P1, 4e-3, 1000)
ax.loglog(f_rms, np.sqrt(P1_rms/1e12)*g1, linestyle='--', linewidth =
    ↵ linewidth, color = l1[0].get_color())
f_rms, P2_rms = rmsnator(f, P2, 4e-3, 1000)
ax.loglog(f_rms, np.sqrt(P2_rms/1e12)*g2, linestyle='--', linewidth =
    ↵ linewidth_2, color = l2[0].get_color())
f_rms, P3_rms = rmsnator(f, P3, 4e-3, 1000)
ax.loglog(f_rms, np.sqrt(P3_rms/1e12)*g3, linestyle='--', linewidth =
    ↵ linewidth_2, color = l3[0].get_color())
f_rms, P4_rms = rmsnator(f, P4, 4e-3, 1000)
ax.loglog(f_rms, np.sqrt(P4_rms/1e12)*g4, linestyle='--', linewidth =
    ↵ linewidth, color = l4[0].get_color())
f_rms, P5_rms = rmsnator(f, P5, 4e-3, 1000)
ax.loglog(f_rms, np.sqrt(P5_rms/1e12)*g5, linestyle='--', linewidth =
    ↵ linewidth_2, color = l5[0].get_color())

ax.set_xlabel("Frequency [Hz]")
ax.set_ylabel(r"Displacement ASD [m/$\sqrt{\text{Hz}}$]")
ax.set_xlim(5e-3, 400)
ax.set_ylim(1e-9, 1e-6)

# Set major ticks at 10^{-13}, ..., 10^{-6}
plt.gca().yaxis.set_major_locator(LogLocator(base=10.0, subs=[1.0],
    ↵ numticks=11))

# Set minor ticks at 2^{-9} x 10^{-n}

```

```
plt.gca().yaxis.set_minor_locator(LogLocator(base=10.0, subs=np.arange(1,
↪ 10)*0.1, numticks=100))

ax.grid(True, 'major', alpha=0.5, linewidth=1)
ax.grid(True, 'minor', alpha=0.2)
ax.set_title('CPS noise preliminary test for different cables and boards')
plt.tight_layout()
handles, labels = plt.gca().get_legend_handles_labels()
plt.legend(loc='upper right', fontsize=10)
plt.show()
```